The Astrophysical Journal Supplement Series, 282:22 (26pp), 2026 January https://doi.org/10.3847/1538-4365/ae1d5f

A Comprehensive Hadronic Code Comparison for Active Galactic Nuclei

Matteo Cerruti[1], Annika Rudolph[2,3], Maria Petropoulou[4,5], Markus Böttcher[6], Stamatios I. Stathopoulos[4,5], Foteini Oikonomou[7], Stavros Dimitrakoudis[4,5], Anton Dmytriiev[6,8], Shan Gao[2], Susumu Inoue[9,10,11], Apostolos Mastichiadis[4], Kohta Murase[12,13], Anita Reimer[14], Joshua Robinson[6], Xavier Rodrigues[15,16], Walter Winter[2], and Andreas Zech[8]

[1] Université Paris Cité, CNRS, Astroparticule et Cosmologie, F-75013 Paris, France; cerruti@apc.in2p3.fr
[2] Deutsches Elektronen-Synchrotron DESY, Platanenallee 6, 15738 Zeuthen, Germany; contact-am3@desy.de
[3] Niels Bohr International Academy and DARK, Niels Bohr Institute, University of Copenhagen, Blegdamsvej 17, 2100, Copenhagen, Denmark
[4] Department of Physics, National and Kapodistrian University of Athens, University Campus Zografos, GR 15784, Athens, Greece; mpetropo@phys.uoa.gr, stamstath@phys.uoa.gr
[5] Institute of Accelerating Systems & Applications, University Campus Zografos, Athens, Greece
[6] Centre for Space Research, North-West University, Private Bag X6001, Potchefstroom 2520, South Africa; markus.boettcher@nwu.ac.za
[7] Department of Physics, Norwegian University of Science and Technology, Høgskoleringen 5, Trondheim 7491, Norway
[8] Laboratoire Univers et Théories, Observatoire de Paris, Université PSL, CNRS, Université Paris Cité, 92190 Meudon, France
[9] Faculty of Education, Bunkyo University, Koshigaya, Japan
[10] Astrophysical Big Bang Laboratory, RIKEN, Wako, Japan
[11] Interdisciplinary Theoretical and Mathematical Sciences Program (iTHEMS), RIKEN, Wako, Japan
[12] Department of Physics and Department of Astronomy & Astrophysics, Penn State University, University Park, PA, USA
[13] Yukawa Institute for Theoretical Physics, Kyoto, Kyoto 606-8502, Japan
[14] Institut für Astro- und Teilchenphysik, Leopold-Franzens-Universität Innsbruck, A-6020 Innsbruck, Austria
[15] Excellence Cluster ORIGINS, Boltzmannstr. 2, D-85748 Garching bei München, Germany
[16] European Southern Observatory, Karl-Schwarzschild-Str. 2, Garching bei München D-85748, Germany
Received 2024 December 6; revised 2025 September 26; accepted 2025 October 3; published 2026 January 9

Abstract

We perform the first dedicated comparison of five hadronic codes (AM^3, ATHEνA, B13, LeHa-Paris, and LeHaMoC) that have been extensively used in modeling the spectral energy distribution (SED) of jetted active galactic nuclei. The purpose of this comparison is to identify the sources of systematic errors (e.g., implementation method of proton–photon interactions) and to quantify the expected dispersion in numerical SED models computed with the five codes. The outputs from the codes are first tested in synchrotron self-Compton scenarios that are the simplest blazar emission models used in the literature. We then compare the injection rates and spectra of secondary particles produced in pure hadronic cases with monoenergetic and power-law protons interacting on blackbody and power-law photon fields. We finally compare the photon SEDs and the neutrino spectra for realistic proton-synchrotron and leptohadronic blazar models. We find that the codes are in excellent agreement with respect to the spectral shape of the photons and neutrinos. There is a remaining spread in the overall normalization that we quantify, at its maximum, at the level of ±40%. This value should be used as an additional, conservative, systematic uncertainty term when comparing numerical simulations and observations.

Unified Astronomy Thesaurus concepts: Active galactic nuclei (16); Radiative transfer simulations (1967); Computational astronomy (293)

1. Introduction

Among the most important open questions in astrophysics is the origin of cosmic rays. They are observed on Earth as a flux of high-energy (up to 10^{20} eV; A. Aab et al. 2020), charged particles, mainly protons and light nuclei (M. Aguilar et al. 2021). Despite extensive searches, the quest for the loci of cosmic-ray acceleration in the Universe remains without a clear answer, especially for the highest energies. Direct searches face the problem that cosmic rays cannot travel on geodesics due to their electric charge, and are deflected in their journey to Earth by magnetic fields. Whenever protons (hadrons) are accelerated to relativistic energies, they can produce energetic secondary particles (pairs, photons, and neutrinos) through inelastic interactions with low-energy photons and matter that are both commonly found in astrophysical sources. Indirect searches for cosmic-ray accelerators are thus based on the detection of the accompanying high-energy photon fluxes escaping their sources (Cherenkov Telescope Array Consortium et al. 2019; J. McEnery et al. 2019).

Indirect cosmic-ray searches face, however, a major issue: how can we be sure that the photons we are observing have been produced by hadrons? Leptons (mainly electrons and positrons) can also emit high-energy photons, and in the large majority of astrophysical sources, the two emissions cannot be easily disentangled. The *leptonic* versus *hadronic* discussion is a recurrent topic in high-energy astrophysical studies. This degeneracy can be broken if we also detect neutrinos from the same object. Neutrinos are naturally produced in hadronic interactions together with photons due to the production and decay of pions. On the other hand, they cannot be produced by leptonic radiative processes, and they can thus be seen as the *smoking gun* for the acceleration of hadrons by an astrophysical object, providing key information such as the maximum energy of the accelerated hadrons and their total power. This multimessenger path has been recently opened

with the detection of a diffuse flux of astrophysical neutrinos by IceCube (M. G. Aartsen et al. 2014). While the gamma–neutrino connection is the most obvious approach to study cosmic-ray accelerators, such multimessenger observations are still limited: so far the best candidates are the 3σ association between a high-energy neutrino detected by IceCube and a gamma-ray flare from the blazar TXS 0506+056 (IceCube Collaboration et al. 2018a), the 3.5σ excess in neutrinos coming from the same source during 2014–2015 (IceCube Collaboration et al. 2018b), and the 4.2σ neutrino excess from the Seyfert galaxy NGC 1068 (IceCube Collaboration et al. 2022).

Well before the detection of high-energy astrophysical neutrinos, hadronic radiative models have been developed to fit multiwavelength observations, both in Galactic (see L. O. Drury et al. 1994; M. G. Baring et al. 1999, for hadronic emission in supernova remnants) and extragalactic sources (see K. Mannheim 1993; F. A. Aharonian 2000; A. Mücke & R. J. Protheroe 2001 for blazars; see M. Böttcher & C. D. Dermer 1998; B. Zhang & P. Mészáros 2001 for gamma-ray bursts (GRBs); see T. A. D. Paglione et al. 1996; H. J. Völk et al. 1996 for starburst galaxies). A considerable effort has been devoted to identifying specific spectral and time properties of hadronic models that can be used to discriminate them from leptonic ones (A. Mücke et al. 2003; M. Böttcher 2005; S. Dimitrakoudis et al. 2012; M. Petropoulou & A. Mastichiadis 2012; M. Böttcher et al. 2013; A. Mastichiadis et al. 2013; C. Diltz et al. 2015; A. Zech et al. 2017). Unfortunately, hadronic radiative models are intrinsically more numerically challenging compared to leptonic ones. In the latter, the main radiative processes are the well-known synchrotron radiation, inverse Compton scattering, and relativistic bremsstrahlung (the latter being important in the modeling of high-density sources like starburst galaxies and supernova shocks propagating in dense circumburst media). In hadronic processes, there is the additional complex task of the computation of the interactions of relativistic protons with low-energy photons and/or matter. In both cases, the final outcome is the production of pions that then decay into photons, leptons, and neutrinos. Photons and leptons can then trigger pair cascades in the emitting region via photon–photon pair production, thus producing more targets for proton–photon interactions. Hadronic source models are intrinsically nonlinear problems, involving physical processes operating typically on vastly different timescales. The numerical complexity of hadronic models in high-energy astrophysics also explains why they have been relatively less investigated compared to leptonic ones. In addition, while a numerical leptonic radiative code can be checked with simple analytical formulae, in hadronic models, these first-order analytical approximations are not always available or have limited applicability.

A clear missing step in the scientific literature is a systematic comparison of numerical codes to estimate the degree of precision reached by current numerical models. This step is particularly urgent at the dawn of the multimessenger gamma–neutrino astrophysics, now that we can test theoretical models and compare their predicted neutrino rates with the observations performed by current neutrino telescopes. The goal of this work is to perform the first comprehensive comparison of five numerical leptohadronic codes published in the scientific literature, discuss the differences in their numerical implementation of hadronic interactions, and estimate their agreement in various parts of the parameter space. As a first part of this project, we limit ourselves to parameters relevant to blazar modeling. In addition, we include a comparison of the numerical neutrino spectra against those obtained with simple analytical approximations often used in the literature. We release all outputs from the five codes for all the tests we performed, as online material, to be used for benchmarking of new codes.

The paper is organized as follows: in Section 2 we describe one-zone blazar emission models and their parameters; in Section 3 we describe the five codes and the effect of numerical resolution on the outputs of individual codes; in Section 4 we describe the tests we performed; in Section 5 we show the results of the code comparison; in Section 6 we discuss nonlinear scenarios; in Section 7 we discuss the results of the code comparison, and we summarize the conclusions of this work. In the appendices, we provide details on the semianalytical neutrino calculation (Appendix A); additional tests we performed (Appendix B); and also, details on how Bethe–Heitler pair production is implemented in ATHEνA and LeHaMoC (Appendix C).

2. One-zone Blazar Emission Models

Blazars are a subclass of jetted (radio-loud) active galactic nuclei (AGNs) characterized by nonthermal emission from radio to gamma rays, a high degree of polarization, and rapid variability, which may be as short as a few minutes (F. Aharonian et al. 2007). Blazars are observed at all wavelengths and are remarkably the most common extragalactic source type in the gamma-ray sky. The name *blazar* is a portmanteau word, from BL Lacertae (a source initially incorrectly classified as a peculiar star, hence its variable star name) and quasars, explicitly reminding us of their blazing behavior. In the framework of the AGN unified model, blazars are understood as the observational effect of a radio-loud AGN whose relativistic jet of plasma launched by the supermassive black hole points toward the observer (C. M. Urry & P. Padovani 1995). Due to the relativistic motion of the emitting plasma, the emission is Doppler boosted in the observer's frame, making these objects much brighter than their parent radio galaxies. Given that only the emission from the jet is boosted, this interpretation explains why blazar emission is dominated by a nonthermal component that outshines all other known AGN radiative components, such as the thermal emission from the accretion disk, the broad and narrow emission lines, and the X-ray corona (P. Padovani et al. 2017).

Spectral energy distributions (SEDs) of blazars are also peculiar among astrophysical objects: the nonthermal emission, while spanning almost 20 orders of magnitude in energy, is pretty simple with two well-separated components, the first one peaking in infrared to X-rays, the second one peaking in gamma rays (MeV to TeV). The position of the peaks varies not only within the blazar population (hence prompting further classifications in X-ray and radio selected blazars; P. Padovani & P. Giommi 1995), or in low-, intermediate-, or high-frequency peaked blazars (A. A. Abdo et al. 2010), but also in a single blazar as a function of the flux state (see M. Baloković et al. 2016, for a study of Mrk 421). The origin of the low-energy SED component is well understood and interpreted as synchrotron radiation by a population of electrons (and positrons) in the relativistic jet. This interpretation is

observationally supported by the detection of a polarized component from radio up to X-rays (see L. Di Gesu et al. 2022, for Mrk 421), by the broadband measurements of the spectral shape of the emission, and by the detection of the core shift effect due to synchrotron self-absorption. The origin of the second, high-energy, SED component is less clear, and falls into the *leptonic* versus *hadronic* dispute discussed in the Introduction. In leptonic blazar models, the high-energy emission is due to inverse Compton scattering, while in hadronic blazar models, it is due to proton synchrotron radiation, and/or synchrotron radiation by secondary particles produced in proton–photon or proton–proton interactions (see M. Cerruti 2020, for a recent review). It is important to underline that even in hadronic models, the first SED component is still explained as synchrotron emission by leptons: the *hadronic* term refers here to the type of accelerated particles responsible (directly or indirectly) for the high-energy part of the blazar SED.

The simplest model for blazar emission considers an emitting region in the jet moving toward the observer with a Doppler factor δ. To further simplify the modeling, a spherical geometry (in the jet rest frame) is commonly assumed, with the radius R as its only parameter. To explain blazar emission, two additional ingredients are needed: the magnetic field strength B in the emission region, and a population of relativistic particles. As discussed above, in the radio band, the synchrotron emission is absorbed due to synchrotron self-absorption, and emission from this single region in the jet cannot reproduce radio observations. Therefore, *one-zone* blazar models consider a single zone in the jet for producing the observed SED, with the notable exception of the radio, which is treated as an upper flux limit in the fit. It is important to underline that the theoretical framework behind one-zone models is not that there is a single, immutable, radiating sphere of plasma in the jet, but rather that, at any given moment, the blazar SED is *dominated* by the emission from one zone. In their simplicity, one-zone models have been successful in explaining the emission from blazars, both for the broadband SEDs and for the time variability and multiwavelength correlations. Exceptions exist, and in particular the detection of objects with unusual SEDs, orphan flares (eruptions seen only in a limited energy band, see, e.g., H. Krawczynski et al. 2004), or the observations of peculiar multiwavelength correlations (e.g., V. A. Acciari et al. 2020), often result in extensions toward multizone emission scenarios (e.g., Z.-R. Wang et al. 2022).

3. The Codes

In this section, we give a brief alphabetically ordered overview of the codes participating in this study. We also provide notes on the development history and astrophysical applications. The physical processes included in the numerical codes are summarized in Table 1. The details on the implementation of hadronic interactions are provided in Table 2.

3.1. AM^3

AM^3 (M. Klinger et al. 2024) is a time-dependent code that solves the coupled kinematic equations of electrons, positrons, photons, protons, neutrons, neutrinos, muons, and pions homogeneously distributed in a comoving volume V of radius R. The code solves the time- and energy-dependent density distribution of each particle species i following a differential equation of the form

$$\partial_t n_i(\gamma, t) = -\partial_\gamma \dot{\gamma}_i(\gamma, t) n_i(\gamma, t) - \alpha_i(\gamma, t) n_i(\gamma, t) + Q_i(\gamma, t), \quad (1)$$

where the $\dot{\gamma}$ terms encode energy loss processes, as listed below, the α_i are sink terms that encode processes leading to particle disappearance, including physical escape from the region and any interactions that destroy particles of species i, and the Q_i are source terms that encode particle injection, including the injection of primary species by the user and interactions that create particles of species i. In this notation, α_i, Q_i, and $\dot{\gamma}_i$ represent the sum over all processes j for species i ($\alpha_i = \sum_j \alpha_i^j$, and so on). For electrons, positrons, and photons, the dimensionless energy is given by $\gamma = E/(m_e c^2)$; and for protons, neutrons, neutrinos, pions, and muons, by $\gamma = E/(m_{p\,[\mathrm{GeV}]})$.

The $\dot{\gamma}$-, α-, and Q-terms encode the following processes:

1. Injection of primary particles with an arbitrary distribution (Q^{inj}).
2. Particle escape (α^{esc}).
3. Synchrotron emission by charged particles, including pions and muons ($\dot{\gamma}_{\mathrm{e}^\pm}^{\mathrm{syn}}$, $\dot{\gamma}_{\mathrm{p}}^{\mathrm{syn}}$, $\dot{\gamma}_{\pi^\pm}^{\mathrm{syn}}$, $\dot{\gamma}_{\mu^\pm}^{\mathrm{syn}}$, $Q_{\mathrm{phot}}^{\mathrm{syn}}$ from $e^\pm$, $\pi^\pm$, $\mu^\pm$, and p).
4. Synchrotron self-absorption ($\alpha_{\mathrm{phot}}^{\mathrm{ssa}}$).
5. Inverse Compton radiation from $e^\pm$ and p ($\dot{\gamma}_{\mathrm{e}^\pm}^{\mathrm{ic}}$,s $\alpha_{\mathrm{phot}}^{\mathrm{ic}}$, $Q_{\mathrm{phot}}^{\mathrm{ic}}$).
6. Photon–photon annihilation ($\alpha_{\mathrm{phot}}^{\mathrm{pp}}$, $Q_{\mathrm{e}^\pm}^{\mathrm{pp}}$).
7. Proton–photon pion production ($\alpha_{\mathrm{phot}}^{\mathrm{p}\gamma\pi}$, $Q_{\mathrm{phot}}^{\mathrm{p}\gamma\pi}$, $\alpha_{\mathrm{p}}^{\mathrm{p}\gamma\pi}$, $Q_{\mathrm{p}}^{\mathrm{p}\gamma\pi}$, $Q_{\pi}^{\mathrm{p}\gamma\pi}$).
8. Neutron–photon pion production ($\alpha_{\mathrm{phot}}^{\mathrm{n}\gamma\pi}$, $Q_{\mathrm{phot}}^{\mathrm{n}\gamma\pi}$, $\alpha_{\mathrm{n}}^{\mathrm{n}\gamma\pi}$, $Q_{\mathrm{n}}^{\mathrm{n}\gamma\pi}$, $Q_{\pi}^{\mathrm{n}\gamma\pi}$).
9. Proton–photon (or Bethe–Heitler, BH) pair production ($\alpha_{\mathrm{phot}}^{\mathrm{BH}}$, $\dot{\gamma}_{\mathrm{p}}^{\mathrm{BH}}$, $Q_{\mathrm{e}^\pm}^{\mathrm{BH}}$).
10. Pion and muon decay kinematics and resulting neutrino emission ($\alpha_{\mu^\pm}^{\mathrm{dec}}$, $\alpha_{\pi^\pm}^{\mathrm{dec}}$, $Q_{e^\pm}^{\mathrm{dec}}$, $Q_{\mu^\pm}^{\mathrm{dec}}$, Q_{ν}^{dec}).
11. Adiabatic cooling of charged particles (α^{ad}, $\dot{\gamma}^{\mathrm{ad}}$).

For the numerical computation, Equation (1) is rewritten in terms of logarithmic energy $x = \ln\gamma$:

$$\partial_t n(x, t) = -\partial_x A(x, t) n(x, t) - \alpha(x, t) n(x, t) + \epsilon(x, t), \quad (2)$$

with the differential number density $n(x) = \gamma n(\gamma)$. The physical processes outlined above are implemented as A, α, and ϵ terms in Equation (2), which can be derived from the initial physical quantities in Equation (1) as

$$A(x) = \frac{\dot{\gamma}}{\gamma}, \quad \epsilon(x) = \gamma Q(\gamma), \quad \alpha(x) = \alpha(\gamma). \quad (3)$$

AM^3 solves Equation (2) for discrete, equally spaced values of x, resulting in logarithmically spaced values of γ. The spacing is fixed to $x_{i+1} - x_i \equiv \ln(\gamma_{i+1}/\gamma_i) = 0.1$, corresponding to 23 bins per energy decade. The code uses three separate energy grids for three different particle groups: a leptonic one for electrons and positrons, a hadronic one for protons, neutrons, pions, muons, and neutrinos, and one for

Table 1
Physical Processes Included in the Numerical Codes

Physical Processes	Codes				
	AM^3	ATHEνA	B13	LeHa-Paris	LeHaMoC
Electron synchrotron radiation	✓	✓	✓	✓	✓
Synchrotron self-absorption	✓	✓	✓	✓	✓
Electron inverse Compton scattering	✓	✓	✓	✓	✓
Electron–positron annihilation	✗	✓	✓	✗	✗
Photon–photon pair production	✓	✓	✓	✓	✓
Triplet pair production	✗	✓	✗	✗	✗
Proton synchrotron radiation	✓	✓	✓	✓	✓
Proton inverse Compton scattering	✓	✗	✗	✗	✗
Proton–photon pair production	✓	✓	✗	✓	✓
Proton–photon pion production	✓	✓	✓	✓	✓
Proton–proton pion production	✗	✗	✗	✓	✓
Neutron–photon pion production	✓	✓	✗	✗	✗
Neutron decay	✗	✓	✗	✗	✗
Kaon synchrotron radiation	✗	✓	✗	✗	✗
Pion synchrotron radiation	✓	✓	✗	✗	✗
Muon synchrotron radiation	✓	✓	✗	✓	✗

Table 2
Main Features of Numerical Codes and Implementation of Hadronic Processes

Features	Codes				
	AM^3	ATHEνA	B13	LeHa-Paris	LeHaMoC
Steady state	✓	✓	✓	✓	✓
Time dependent	✓	✓	✗	✗	✓
Linear cascades	✓	✓	✓	✓	✓
Nonlinear cascades	✓	✓	✗	✗	✓
Implementation					
Photo-pion process	Following Ref. (a)	Tabulated SOPHIA (b)	Following Ref. (c)	Running SOPHIA (b)	Following Ref. (c)
Photo-pair process	Following Ref. (c)	Tabulated from Ref. (d)	n/a	Following Ref. (c)	Following Ref. (c)

References. (a) S. Hummer et al. (2010), (b) A. Mücke et al. (2000), (c) S. R. Kelner & F. A. Aharonian (2008), (d) R. J. Protheroe & P. A. Johnson (1996).

photons. The leptonic and hadronic grids start from cold particles, i.e., with $\gamma = 1$ ($x_0 = \ln(1)$). The maximum value of each of the three grids, as well as the minimum value of the photon grid, can be defined by the user upon initialization. The particle densities are computed in units of cm^{-3} for protons, neutrons, pions, muons, and neutrinos, and in units of $\sigma_T^{3/2}$ for electrons, positrons, and photons, where σ_T is the Thomson scattering cross section.

The system is evolved linearly in time t. The size of the time step Δt is defined by the user upon initialization, and can be subsequently redefined at any moment during the simulation. At every time t, AM^3 automatically selects the algorithm to be deployed when calculating the subsequent step, as detailed further in M. Klinger et al. (2024). In summary, if the energy loss terms in Equation (2) dominate over the sink terms or vice versa ($A(x, t) \gg \alpha(x, t)$ or $A(x, t) \ll \alpha(x, t)$), the nondominant terms are neglected and an analytical approximation is deployed when calculating $n(x, t + \Delta t)$, increasing the efficiency of the code. If both terms are of comparable magnitude, the full numerical solver is deployed using a tridiagonal matrix method based on a semi-implicit scheme in x (T. Chang & G. Cooper 1970) and a Crank–Nicolson scheme in t. The solver updates the coefficients for each species at time t, including the integration over energy distributions of target particles when applicable, as in the case of Compton scattering or hadronic interactions. The particle spectrum is then evolved forward by Δt. The new density value $n(x, t + \Delta t)$ is calculated, as well as the new coefficients $A(x, t + \Delta t)$ and $\alpha(x, t + \Delta t)$. The user is responsible for choosing a sufficiently small value of Δt to maintain accuracy, especially in optically thick regimes, which requires testing the stability of the solution.

The treatment of processes 1–6 for leptons, positrons, and protons is described in detail in I. Vurm & J. Poutanen (2009) and S. Gao et al. (2017). The synchrotron photon emission and respective cooling timescale also include the quantum synchrotron regime (following J. J. Brainerd 1987), which is relevant in the presence of strong magnetic fields. Bethe–Heitler pair production is calculated following the treatment by S. R. Kelner & F. A. Aharonian (2008), with the cross section given by Equation (10) of G. R. Blumenthal & R. J. Gould (1970), valid in the Born limit (see M. Klinger et al. 2024), and the expression for the energy loss term given by Equation (9.35) of C. D. Dermer & G. Menon (2009). For photon-proton and photon-neutron pion production, the code follows the procedure outlined by S. Hummer et al. (2010), based on SOPHIA (A. Mücke et al. 2000). In Section 5.2, we provide further details on the approach, including the methods used for performance optimization. Neutral pions are not included as an individual species but are assumed to decay instantaneously,

while charged pions are treated as individual species that undergo escape and cooling, emit synchrotron radiation, and decay. The same is true for the unstable, intermediate muons emerging from pion decay. The neutrino emission rates are calculated at each time step based on the current pion and muon densities.

The code has been applied to time-dependent multiwavelength studies of AGN (e.g., S. Gao et al. 2017, 2019; X. Rodrigues et al. 2021, 2024a, 2024b; G. Fichet de Clairfontaine et al. 2023), and more recently to the prompt and afterglow phases of GRBs (A. Rudolph et al. 2022, 2023a, 2023b; M. Klinger et al. 2024) and tidal disruption events (C. Yuan & W. Winter 2023; C. Yuan et al. 2024a, 2024b).

3.2. ATHEνA

ATHEνA is a time-dependent leptohadronic radiative transfer code, which was first presented in A. Mastichiadis & J. G. Kirk (1995). Since then, it has been updated in various ways and evolved to its current form (for details, see A. Mastichiadis et al. 2005; S. Dimitrakoudis et al. 2012; M. Petropoulou et al. 2014b). The numerical code solves a system of coupled integrodifferential equations that describe the evolution of five particle distributions within a fixed spherical volume (of radius R), namely relativistic protons, relativistic neutrons, relativistic electrons and positrons, photons, and neutrinos. The equation of each one of the above particle distributions can be written in the following compact form:

$$\frac{\partial n_i(x_i,\,t)}{\partial t} + \frac{n_i(x_i,\,t)}{t_{i,\rm esc}(x_i)} + \sum_j \mathcal{L}_i^j(x_i,\,t) = \sum_j \mathcal{Q}_i^j(x_i,\,t) + \mathcal{Q}_i^{\rm inj}(x_i,\,t), \tag{4}$$

where t is time (in units of R/c), n_i is the differential number density (normalized to $\sigma_{\rm T}R$) of particle species i, x_i is the particle dimensionless energy (in units of m_ic^2), $t_{i,\rm esc}$ is the particle escape timescale (also in units of R/c), $\mathcal{L}_i^j$ is the operator for particle losses (sink term) due to process j, $\mathcal{Q}_i^j$ is the operator of particle injection (source term) due to process j, and $\mathcal{Q}_i^{\rm inj}$ is the operator of a generic external injection. The coupling of the equations happens through the energy loss and injection terms for each particle species. When the differential energy loss rate for a particle species i due to process j is integrated over the particle energy grid, it equals the bolometric energy injection rate to particle species i' due to the same process,

$$\int dx\, x\mathcal{L}_i^j(x,\,t) = \int dx\, x\mathcal{Q}_{i'}^j(x,\,t). \tag{5}$$

This guarantees, at least formally, that the total energy lost by one particle species (e.g., protons) equals the energy transferred to other particles (e.g., pairs, neutrinos, and photons).[17]

The physical processes that are included in the code are:

1. Electron synchrotron radiation ($\mathcal{L}_e^{\rm syn}$, $\mathcal{Q}_\gamma^{\rm syn}$).
2. Synchrotron self-absorption ($\mathcal{L}_\gamma^{\rm ssa}$).
3. Electron inverse Compton scattering ($\mathcal{L}_e^{\rm ic}$, $\mathcal{Q}_\gamma^{\rm ic}$).
4. Electron–positron annihilation ($\mathcal{L}_e^{\rm ann}$, $\mathcal{Q}_\gamma^{\rm ann}$).
5. Photon–photon ($\gamma\gamma$) pair production ($\mathcal{Q}_e^{\gamma\gamma}$, $\mathcal{L}_\gamma^{\gamma\gamma}$).
6. Photon Compton downscattering on cold pairs.
7. Triplet pair production ($\mathcal{L}_e^{\rm tpp}$, $\mathcal{Q}_e^{\rm tpp}$).
8. Proton synchrotron radiation ($\mathcal{L}_p^{\rm syn}$, $\mathcal{Q}_\gamma^{\rm psyn}$).
9. Proton–photon (Bethe–Heitler) pair production ($p\gamma e$; $\mathcal{L}_p^{p\gamma e}$, $\mathcal{Q}_e^{p\gamma e}$).
10. Proton–photon pion production ($p\gamma\pi$; $\mathcal{L}_p^{p\gamma\pi}$, $\mathcal{Q}_\gamma^{p\gamma\pi}$, $\mathcal{Q}_e^{p\gamma\pi}$, $\mathcal{Q}_\nu^{p\gamma\pi}$, $\mathcal{Q}_n^{p\gamma\pi}$).
11. Neutron–photon pion production ($n\gamma\pi$; $\mathcal{L}_n^{n\gamma\pi}$, $\mathcal{Q}_p^{n\gamma\pi}$).
12. Neutron decay.

Leptonic processes 1–6 are modeled as described in A. Mastichiadis & J. G. Kirk (1995), except for the photon production and electron energy loss operators for inverse Compton scattering. The inverse Compton photon production operator is calculated according to Equation (2.48) of G. R. Blumenthal & R. J. Gould (1970), which applies to the Thomson and Klein–Nishina scattering regimes. The electron loss operator due to scatterings in the Klein–Nishina regime is given by the third and fourth terms on the left-hand side of Equation (5.7) in G. R. Blumenthal & R. J. Gould (1970). The probability $P(E, E')$ of an electron with energy E to emit a photon of energy $E - E'$ that enters in these terms is computed according to Equation (5.17) of G. R. Blumenthal & R. J. Gould (1970). Triplet pair production was modeled according to A. Mastichiadis (1991) (see also, M. Petropoulou et al. 2019). Proton–photon (photohadronic) interactions are modeled using the results of Monte Carlo simulations. In particular, for Bethe–Heitler pair production, the Monte Carlo results by R. J. Protheroe & P. A. Johnson (1996) were used (for more details on the implementation, see A. Mastichiadis et al. 2005 and Appendix C). Photo-pion interactions were incorporated in the time-dependent code by using the results of the Monte Carlo event generator SOPHIA (A. Mücke et al. 2000), which takes into account channels of multipion production for interactions much above the threshold (for more details see S. Dimitrakoudis et al. 2012).

We also include the effects of kaon, pion, and muon synchrotron losses, albeit in a way that does not require the use of additional kinetic equations. Pion ($\pi^\pm$, π^0), charged and neutral (K_S^0 and K_L^0) kaon production rates from photomeson interactions have been computed by the SOPHIA event generator (A. Mücke et al. 2000). For each particle energy, we calculate the energy lost to synchrotron radiation before it decays. The remainder of that energy is then instantaneously transferred to the particle's decay products, whose yields have also been computed by the SOPHIA event generator. Since the secondary particles from kaon decay include pions, we first calculate charged kaon decay and then charged pion decay. Finally, the same process is applied to the resulting muons. The photons, electrons, and neutrinos resulting from kaon, pion, and muon decay are added as production rates to their respective kinetic equations, as are the photons from kaon, pion, and muon synchrotron radiation. Neutral kaons (K_S^0 and K_L^0) and pions (π^0) are, as in S. Dimitrakoudis et al. (2012), assumed to decay instantaneously, therefore directly contributing their decay products to the kinetic equations.

[17] Because the integration is performed on discretized functions, Equation (5) cannot ensure exact energy conservation. In practice, the two integrals agree to within approximately 1%–10% (depending on the physical process and input parameters) for the default code settings. If stricter energy conservation is required, the user can choose to renormalize the energy injection rates to match the corresponding energy loss rates for all processes.

Table 3
Energy Grid Specifications of Each Code, Used in the Case Studies Presented in This Work

	AM[3]	ATHEνA	B13	LeHa-Paris	LeHaMoC
Electron energy grid					
Number of points or points per decade	23/decade	10/decade	150 points	200 points	30/decade
Minimum grid energy/$(m_e c^2)$	1.0	$10^{0.1}$	1.0	1.0	1.0
Maximum grid energy/$(m_e c^2)$	5.3×10^{14}	10^{13}	1.0×10^{12}	1.0×10^{8}	10^{11}
Proton energy grid					
Number of points or points per decade	23/decade	10/decade	300 points	200 points	10/decade
Minimum grid energy/$(m_p c^2)$	1.0	$10^{0.1}$	1.0	1.0	1.0
Maximum grid energy/$(m_p c^2)$	4.3×10^{13}	10^{11}	1.0×10^{10}	1.0×10^{10}	10^{9}
Photon energy grid					
Number of points or points per decade	23/decade	20/decade	250 points	200 points	10/decade
Minimum grid frequency [Hz]	8.53×10^{7}	4.5×10^{7}	$1.2 \times 10^{7} \times B$/G	1.0×10^{9}	$10^{7.5}$
Maximum grid frequency [Hz]	6.55×10^{34}	1.1×10^{33}	1.2×10^{32}	1.0×10^{45}	10^{32}

The remaining particle distributions are modeled by coupled kinetic equations. The code uses equally spaced logarithmic grids for x_i of particle species i (for neutrons we use the same energy grid as protons, while for neutrinos we use the same energy grid as electrons; see Table 3, where the energy grid parameters of each code are specified). An array $y(x, t) = \{n_{\rm p}(x_{\rm p}, t), n_{\rm e}(x_{\rm e}, t), n_{\gamma}(x_{\gamma}, t), n_{\rm n}(x_{\rm n}, t), n_{\nu}(x_{\nu}, t)\}$ is defined, where $x = \{x_{\rm p}, x_{\rm e}, x_{\gamma}, x_{\rm n}, x_{\nu}\}$ denotes the combined energy grid for all species. The code uses the routine d02ejf from the NAG Fortran library, which integrates a stiff system of first-order ordinary differential equations (ODEs) over an interval with suitable initial conditions. The routine uses a variable-order, variable-step method implementing the backward differentiation formulae. More specifically, the routine solves a set of equations of the form $y_i' = f_i(x, y_1, y_2, ..., y_n)$ for $i = 1, 2, \ldots, n$. Here, the prime denotes the time derivative, and n is the number of ODEs, which equals the length of x. The function f_i contains all the injection and loss terms in Equation (5) and is evaluated in time t for $i = 1, 2, \ldots, n$.

The adopted numerical scheme is ideal for studying electromagnetic cascades in both linear and nonlinear regimes,[18] and for simulating time-dependent problems, such as flares. The code has been extensively used in the steady-state or time-dependent modeling of nonthermal radiation from AGN (e.g., A. Mastichiadis & J. G. Kirk 1997; S. Dimitrakoudis et al. 2014; M. Petropoulou et al. 2014c, 2015a, 2016, 2020; D. Karavola & M. Petropoulou 2024; D. Karavola et al. 2025), applied to multimessenger emissions from GRBs (M. Petropoulou et al. 2014a, 2014b; I. Florou et al. 2021), used for the study of pair cascades in electrostatic gaps (M. Petropoulou et al. 2019), and of radiative instabilities in leptohadronic relativistic plasmas (A. Mastichiadis et al. 2005, 2020; M. Petropoulou & A. Mastichiadis 2012; M. Petropoulou et al. 2014a; M. Petropoulou & A. Mastichiadis 2018).

3.3. B13

The leptohadronic code of M. Böttcher et al. (2013) (B13) describes the multiwavelength behavior of blazars in a steady state. This homogeneous one-zone model starts with the injection of a power-law distribution of ultrarelativistic electron–positron pairs and protons into a spherical emission region of size R, which moves with a constant relativistic speed β_Γ corresponding to bulk Lorentz factor Γ. Cooling is performed via synchrotron and Compton emission on various photon fields: The comoving electron synchrotron (synchrotron self-Compton (SSC)) and direct accretion disk radiation as well as an arbitrary external radiation field, assumed to be isotropic in the AGN rest frame. For the latter, a separate routine is used to write the desired isotropic external photon spectrum into an input file, which is then read by the main code. The full Klein–Nishina cross section for inverse Compton scattering is used, adopting the analytical solution of M. Boettcher et al. (1997). In a pure leptonic scenario, the self-consistent radiative output is calculated based on a temporary equilibrium between particle injection $Q(\gamma)$, radiative cooling at a rate $\dot{\gamma}$ and electron escape on a timescale of $t_{\rm esc} = \eta_{\rm esc} R/c$. Given a critical Lorentz factor γ_c, where $\dot{\gamma}(\gamma_c) = \gamma_c/t_{\rm esc}$, an analytical approximation to the equilibrium solution ($\partial_t n(\gamma, t) = 0$) to Equation (1), i.e.,

$$0 = Q(\gamma) - \frac{\partial}{\partial \gamma}(\dot{\gamma}\, n[\gamma]) - \frac{n(\gamma)}{t_{\rm esc}} \tag{6}$$

is evaluated as

$$n(\gamma) = \begin{cases} f_c\, Q(\gamma)\, t_{\rm esc} & \text{for } \gamma \leqslant \gamma_c \\ \dfrac{1}{\dot{\gamma}} \displaystyle\int_{\gamma}^{\infty} Q(\gamma)\, d\gamma & \text{for } \gamma > \gamma_c \end{cases}, \tag{7}$$

where f_c is a normalization constant to ensure continuity of the particle distribution at $\gamma = \gamma_c$. In the fast-cooling regime, where $Q(\gamma)$ has a low-energy cutoff at $\gamma_{\rm min} > \gamma_c$, the $\gamma \leqslant \gamma_c$ branch of Equation (7) is empty and the integral in the $\gamma > \gamma_c$ branch becomes constant for $\gamma \leqslant \gamma_{\rm min}$, i.e., the solution reduces to $n(\gamma) = {\rm const.}/\dot{\gamma}$ for $\gamma_c \leqslant \gamma \leqslant \gamma_{\rm min}$. The resulting particle distribution is normalized to a kinetic power of $L_{\rm kin} = \Gamma^2 \beta_\Gamma mc^3 \pi R^2 \int_1^{\infty} \gamma\, n(\gamma)\, d\gamma$, which is an input parameter. As SSC cooling depends on the self-consistently produced synchrotron radiation field, which, in turn, depends on the equilibrium particle distribution, the code employs an iterative scheme: Starting with an initial guess of $\dot{\gamma}_{\rm SSC} = \dot{\gamma}_{\rm sy}$, it evaluates a first-guess equilibrium distribution, which is then used to calculate the corresponding synchrotron spectrum, based on which a new $\dot{\gamma}_{\rm SSC}$ is evaluated, which is used to calculate a new equilibrium particle distribution. This

[18] If the energy density of the secondary photons is lower than that of the synchrotron photons from primary electrons (and/or external radiation fields), the cascade is considered to be linear, i.e., the interactions between secondary pairs and photons can be neglected. Otherwise, the cascade is characterized as nonlinear or self-supported.

procedure is repeated until the solution converges to a self-consistent equilibrium. In a leptohadronic scenario, the radiative output in a temporary equilibrium is evaluated for both primary electrons and protons, taking internal $\gamma\gamma$ pair production and cascades into account.

For leptohadronic processes (in a stationary state), the code employs the semianalytical expressions of S. R. Kelner & F. A. Aharonian (2008) for the final decay products (electrons, positrons, photons, and neutrinos) from photo-pion interactions. Bethe–Heitler pair production is not included. A semianalytical approach, described in detail in M. Böttcher et al. (2013), is used to evaluate the output due to pair cascades initiated by pairs from pion and muon decay and from photon–photon attenuation of primary gamma rays. The code has been designed to describe stationary SEDs; thus, short-term variability is averaged out over the integration time of the SED. All particle energies and photon frequencies are discretized on regular logarithmic grids, as specified in Table 3, and numerical integrations over particle and frequency distributions are carried out using standard finite-difference schemes. This code has shown robust results on the modeling of Fermi Large Area Telescope–detected blazars (e.g., M. Böttcher et al. 2013).

3.4. LeHa-Paris

The LeHa-Paris code (M. Cerruti et al. 2015) is a steady-state numerical code that computes photon and neutrino emission by a population of electrons and protons at equilibrium in a spherical emitting region in a relativistic jet. The code is built upon the leptonic (SSC) code by K. Katarzyński et al. (2001). A population of primary electrons at equilibrium in the emitting region (assumed spherical, with parameters δ, B, and R) is parameterized by a broken power-law distribution (with parameters $\gamma_{\rm min}$, $\gamma_{\rm break}$, $\gamma_{\rm max}$, $\alpha_{1,2}$, and normalization K). The leptonic part of the code computes synchrotron emission and SSC emission (using the kernel by F. C. Jones 1968). Photon and particle energy vectors are discretized with a logarithmic step, as specified in Table 3. Numerical integrals are computed with a Gauss–Legendre algorithm. A first development of the leptonic part of the code has been the computation of pair injection from $\gamma\gamma$ pair production, which is implemented following F. A. Aharonian et al. (1983). Their steady-state distribution is computed taking into account synchrotron cooling using the integral solution of S. Inoue & F. Takahara (1996), which solves the differential Equation (1) for $\partial_t n_i(\gamma, t) = 0$).

The hadronic part of the code computes synchrotron radiation by protons (which is implemented as for the primary electrons) and proton–photon interactions. The latter are computed assuming that the target photon field is synchrotron emission by primary electrons and protons, and SSC. The energy distributions of secondary particles injected via photo-meson interactions are computed running the Monte Carlo code SOPHIA (A. Mücke et al. 2000). With respect to the public version of SOPHIA, the code is modified to take as input arbitrary target photon fields, to extract as well the muon spectra, and to include the synchrotron cooling of kaons, pions, and muons. SOPHIA outputs are considered as injection terms to compute the steady-state distributions at equilibrium. Photon and neutrino spectra are obtained by multiplying their injection rates times their escape timescale; for leptons, the steady-state distributions are computed as for $\gamma\gamma$ pairs. For muons, the steady-state solution needs to include their decay time, and the explicit integral solution is provided in M. Cerruti et al. (2015). Pair injection from Bethe–Heitler pair production is computed following S. R. Kelner & F. A. Aharonian (2008) and G. R. Blumenthal & R. J. Gould (1970), and their steady state is computed as for other leptons. Pair cascades are computed iteratively: the code computes the steady-state distribution of a leptonic population, its synchrotron and inverse Compton radiation, then computes the pair injection from $\gamma\gamma$ pair production, its steady state, its radiative emission, and so on, until the contribution of the nth generation is negligible. For all applications in this work, the cascades are computed up to the fifth generation included. The explicit assumption is that the cascade is never self-supported and always driven by the synchrotron and SSC photons from the primary electrons, or by the synchrotron photons from the primary protons. In the same way, the emission from the cascade does not affect the distribution of primary electrons and protons.

In the original version of the code, the simulation is limited to a scenario in which external photon fields are negligible, meaning that the dominant soft photon field for $\gamma\gamma$ and pγ interactions is the synchrotron radiation by primary electrons, and that synchrotron cooling is always dominating over inverse Compton cooling. It is thus suited to model emission from high-frequency-peaked BL Lac objects. Besides the original application to extreme blazars, the code has been used to study the potential detection of hadronic spectral features in the TeV band with the Cherenkov Telescope Array Observatory (A. Zech et al. 2017), to model the emission from the peculiar high-luminosity blazar PKS 1424+240 (M. Cerruti et al. 2017), and to model the blazar neutrino candidate TXS 0506+056 (M. Cerruti et al. 2019). As a major upgrade for this project, the code has been extended to be able to deal with external photon fields: an arbitrary photon field (expressed as photon energy density as a function of frequency, in the reference frame of the emitting region) provided by the user is read into the code, and used for the calculation of all radiative processes (inverse Compton emission, Bethe–Heitler pair production and photo-meson interactions). Additionally, the computation of particle distributions at equilibrium takes into account inverse Compton cooling. The augmented version of the code, which now also includes p-p interactions, has already been applied to study blazar neutrino candidates (V. A. Acciari et al. 2022; A. Acharyya et al. 2023) and the multimessenger emission from NGC 1068 (S. Inoue et al. 2022).

3.5. LeHaMoC

LeHaMoC[19] is an open-source, time-dependent leptohadronic code described in S. I. Stathopoulos et al. (2024b). It is designed to solve complex partial differential equations (PDEs) that model the interactions and emissions of particles (kinetic equations) in high-energy astrophysical environments such as blazars. The PDEs account for particle injection, escape, and losses due to physical processes such as synchrotron radiation, inverse Compton scattering, and photo-hadronic interactions. The code accounts for various particle species, including relativistic electrons, positrons, protons,

[19] https://github.com/mariapetro/LeHaMoC/

photons, and neutrinos, within an assumed spherical and potentially expanding region of radius R.

LeHaMoC tackles the coupled integrodifferential equations governing these particle populations (see Equation (4)) by using a combination of finite-difference methods and an implicit time-stepping scheme (T. Chang & G. Cooper 1970), which ensures stability and accuracy over long simulation periods. Stiff differential equations commonly arise in the context of AGN modeling, since the various timescales associated with physical processes can differ by many orders of magnitude across the energy domain. The Chang & Cooper scheme is well suited for the numerical solution of the said problems. To discretize the kinetic equations in time, the user selects a time step that is related to the characteristic timescale of the system. The default choice is $1\ R/c$, but shorter time steps may be needed. The use of an implicit scheme ensures that the solution at any time step is stable, which is useful since the timescales of different physical processes can vary widely. The discretization in energy is achieved by using a logarithmic energy grid that allows us to accurately capture the behavior of the distribution over a wide range of energies. The energy grid size is a parameter that the user can define. Each discretized equation forms a tridiagonal matrix that we solve using the Thomas algorithm (L. H. Thomas 1949).

In LeHaMoC relativistic pairs and protons are injected into power-law distributions, featuring either sharp or exponential cutoffs. The time evolution of these particles is governed by the solution of the coupled kinetic equations. The leptonic processes modeled include synchrotron radiation, synchrotron self-absorption (C. D. Dermer & G. Menon 2009), electron inverse Compton scattering (G. R. Blumenthal & R. J. Gould 1970; A. Mastichiadis & J. G. Kirk 1995), and photon–photon annihilation (A. Mastichiadis & J. G. Kirk 1995). The hadronic processes encompass proton synchrotron radiation, Bethe–Heitler pair production (G. R. Blumenthal & R. J. Gould 1970; S. R. Kelner & F. A. Aharonian 2008), proton–photon pion production (S. R. Kelner & F. A. Aharonian 2008), and the inelastic collisions of relativistic protons with ambient cold protons (S. R. Kelner et al. 2006).

The leptonic part of the code has been used in the modeling of the afterglow emission of GRB 221009A (B. Banerjee et al. 2025) and for the calculation of the pair signatures and distribution in the magnetospheric current sheets in M87* (S. I. Stathopoulos et al. 2024a). The full leptohadronic code, with the inclusion of external photon fields, was employed by S. I. Stathopoulos & M. Petropoulou (2025) to investigate the multimessenger emission of blazar jets powered by magnetic reconnection at various distances from the central supermassive black hole. The time-dependent features of the code are presented in M. Chatzis et al. (2024). This work explores the time-variable behavior of blazar Mrk 501, focusing on identifying hadronic signatures in its photon emission when varying some of the model parameters (i.e., electron/proton luminosity, magnetic field, and the power-law indexes of the distributions) according to simulated light curves.

3.6. Resolution in Codes

In this section, we discuss the effects of energy grid resolution and time step on the results obtained by the different codes, whenever applicable.

In ATHEνA the routine used for the integration of kinetic equations `d02ejf`[20] uses an adaptive time step, which cannot be controlled by the user. However, the resolution in the energy grid of electrons (and protons) is set by the user through the parameter `npdec` (i.e., number of grid points per decade). The photon energy grid is designed to have twice this number of points per decade. While the minimum energy in the proton ($\gamma_{p,\rm min}$) and electron ($\gamma_{e,\rm min}$) grids is typically some factor of 10, the minimum energy in the photon grid is set to $x_{\rm min} = b\gamma^2_{e,\rm min}$, where $b = B/B_c$ and $B_c = m_e^2c^3/e\hbar$. That creates a seamless correspondence of bins when photons are produced by synchrotron radiation but is less ideal for other processes. In neutral pion decay, in particular, the mismatch between the proton and photon grids introduces a small error in the photon spectrum around its peak, since it usually involves only a few bins. Nevertheless, when applying the proton–photon pion production process, `npdec` is always set to 10, so as to align with the SOPHIA tabulated particle distributions with a small degree of smoothing. The latter come in a binning of 20 grid points per decade, so by using 10 points in ATHEνA for most particles and 5 points for photons, we are able to add together the values of two particle bins and four photon bins from SOPHIA. Moreover, the Bethe–Heitler implementation (see Appendix C) is designed only for `npdec` $= 10$. Therefore, the energy resolution in ATHEνA can only be changed in purely leptonic scenarios. We use the example of the inverse Compton catastrophe (Section 6.1) to illustrate the effects of `npdec`, as shown in Figure 1.

In AM^3 the resolution of the energy grid is fixed to $\Delta\log(E) = 0.1$, but the time step of the solver can be selected by the user. The effect of the time step on the accuracy of the results is summarized in Figure 2. We have simulated the Compton catastrophe scenario, using the same parameters as in Section 6.1, and evolving the system to 10 times the dynamical timescale, that is, up to $10\,t_{\rm esc} = 10\,R/c$, to guarantee a steady-state result. For this particular purpose, we ignore the effect of synchrotron self-absorption, which would otherwise lead to significant attenuation of the emitted photon flux, due to the extreme electron density. We tested four different time step sizes, from $\Delta t = 0.1\,t_{\rm esc}$, which is the least computationally demanding down to $10^{-3}\,t_{\rm esc}$, which is the most accurate. The resulting photon spectra and their relative deviations are shown in the left and middle panels, respectively. As we can see, the simulation performed using only 10 time steps per dynamical timescale provides the least accurate results overall, with relative error fluctuating from -8% to $+4\%$. At 200 time steps per dynamical timescale, the maximum absolute error has been reduced to 2%. For any number of steps beyond 1000, the result remains practically unchanged. As we can see on the upper right panel, the number of time steps performed by the solver is directly proportional to the computation time; in that sense, the choice of time step in AM^3 reflects a trade-off between accuracy and computational efficiency.

In LeHa-Paris, there are two resolution effects, one related to the grid used for particles and photons, and one related to the SOPHIA simulations that are run on the fly. The first effect is similar to the other codes, and we do not show it here (for reference, all results presented here have been performed using 200 points for particle and photon distributions). We discuss

[20] https://support.nag.com/numeric/fl/nagdoc_fl24/pdf/d02/d02ejf.pdf

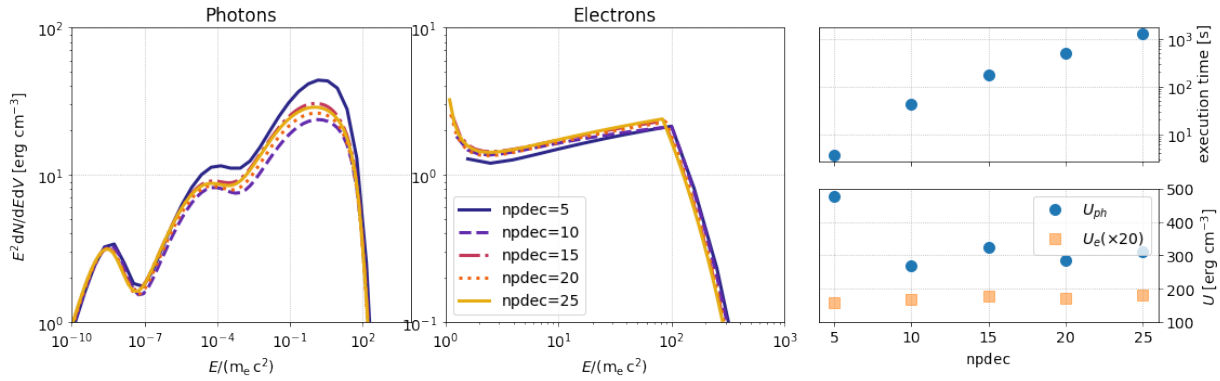

Figure 1. Dependence of results on the resolution of particle energy arrays (`npdec`) used in the ATHEνA code for the Compton catastrophe scenario discussed in Section 6.1. Left panel: photon energy density distribution. Middle panel: electron energy density distribution. Top right: CPU time as a function of `npdec`. Bottom right: integrated photon and electron energy densities plotted against `npdec`. The electron energy density is multiplied by a factor of 20 for display purposes.

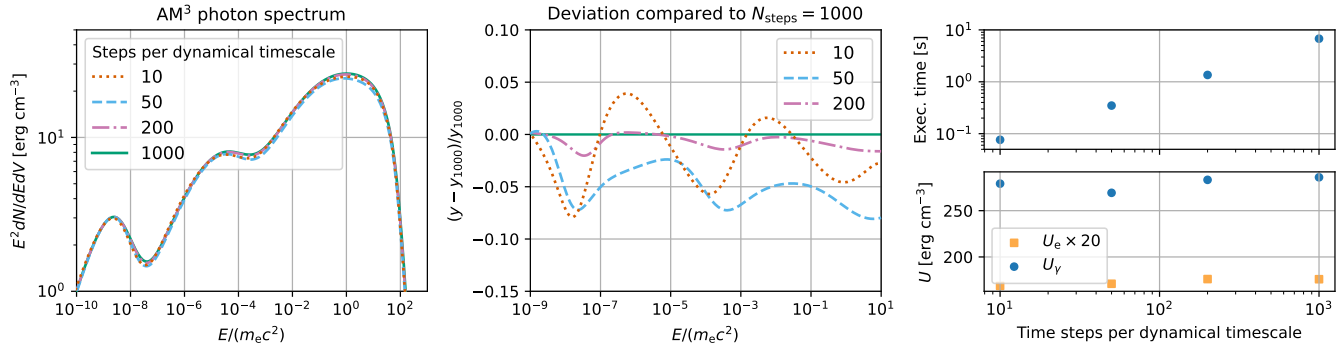

Figure 2. Dependence of AM^3 results on the size of the solver time step selected by the user. Like in Figure 1, we simulate the Compton catastrophe scenario of Section 6.1. Left: steady-state photon energy density, obtained using 10, 50, 200, and 1000 steps per dynamical timescale, which in this case corresponds to the light-crossing time of the system, R/c. Middle: relative ratio between the fluxes shown in the left panel, using as a reference the result obtained with 1000 time steps. Top right: CPU time as a function of the number of time steps. Bottom right: integrated photon and electron energy densities.

here the effect of changing the resolution of the SOPHIA calls. LeHa-Paris uses five parameters to call SOPHIA: the proton distribution is sampled SOPHIA_CALL times, from the maximum proton energy downwards with a SOPHIA_STEP step; for each call, SOPHIA executes SOPHIA_TRIALS independent Monte Carlo realizations of the proton–photon interaction; the outputs for each proton energy are characterized by a SOPHIA_NBINS number of bins with a SOPHIA_DELX step. To correctly sum all outputs, the ratio SOPHIA_STEP over SOPHIA_DELX has to be an integer. In the following, we show the effect of degrading the resolution for the benchmark test pγ-PLPL, looking at the photon injection only. The result shown in Figure 7 has been obtained using SOPHIA_CALL = 200; SOPHIA_STEP = 0.05; SOPHIA_TRIAL = 1000; SOPHIA_NBINS = 200; SOPHIA_DELX = 0.025. In Figure 3, we show the effect of changing SOPHIA_TRIAL to 200 and 50, as well as reducing SOPHIA_CALL to 100.

4. Case Studies

Before discussing the details of the test cases we investigated, we need to comment on several differences in the code definitions and implementations that have to be considered to have a fair comparison of the output results.

AM^3 and ATHEνA are time-dependent codes that take as input the injection rate of particle species i per unit volume, $Q_i^{\rm inj}(\gamma, t)$ (see Equations (1) and (4)). The particle injection rate translates to a bolometric kinetic injection luminosity, $L_i^{\rm inj}$, as

$$L_i^{\rm inj} = \frac{4}{3}\pi R^3 m_i c^2 \int_1^\infty d\gamma\,(\gamma - 1) Q_i^{\rm inj}(\gamma), \tag{8}$$

where $Q_i^{\rm inj}$ may depend on time in the general case. The particle injection compactness, a dimensionless measure of the particle luminosity, is then defined as

$$\ell_i^{\rm inj} \equiv \frac{\sigma_{\rm T} L_i^{\rm inj}}{4\pi R m_i c^3} = \frac{\sigma_{\rm T} R^2}{3c} \int_1^\infty d\gamma\,(\gamma - 1) Q_i^{\rm inj}(\gamma). \tag{9}$$

B13 and LeHa-Paris are steady-state codes, hence they take as input the number density of particle species at steady state, $n_i^{\rm ss}$. In the absence of cooling, the latter quantity is related to the injection compactness as follows:

$$\ell_i^{\rm inj} = \frac{\sigma_{\rm T} R^2}{3ct_{i,\rm esc}} \int_{\gamma_{i,\rm min}}^{\gamma_{i,\rm max}} d\gamma\,(\gamma - 1) n_i^{\rm ss}(\gamma). \tag{10}$$

They take as input the number density at $\gamma = 1$, $n_i^{\rm ss}|_{\gamma=1}$. So, for the commonly used power-law distribution with slope s_i between $\gamma_{i,\rm min}$ and $\gamma_{i,\rm max}$, Equation (10) reads as

$$n_i^{\rm ss}|_{\gamma=1} = \frac{3ct_{i,\rm esc}\ell_i^{\rm inj}}{\sigma_{\rm T} R^2} \begin{cases} \dfrac{2 - s_i}{\gamma_{i,\rm max}^{2-s_i} - \gamma_{i,\rm min}^{2-s_i}} & s_i \neq 2 \\ \ln^{-1}\left(\dfrac{\gamma_{i,\rm max}}{\gamma_{i,\rm min}}\right) & s_i = 2 \end{cases}. \tag{11}$$

The normalization parameters in AM^3 and ATHEνA are originally implemented assuming that the integrands in

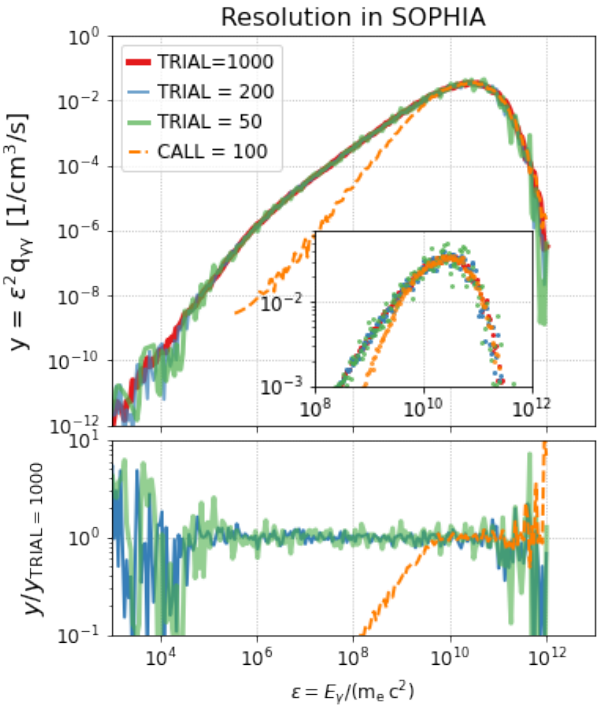

Figure 3. Dependence of results from LeHa-Paris on the resolution of SOPHIA.

Equation (8) and (9) are injected power-law functions with a sharp cutoff at $\gamma_{\rm max}$. For the purpose of this project, all tests have been performed assuming that all primary particle distributions are defined with injected exponential cutoffs at $\gamma_{\rm max}$, with the notable exception of the tests with monoenergetic protons. Still, the normalization of the particle distributions is computed by integrating up to $\gamma_{\rm max}$, even though the exponential cutoff is present in the particle distributions.

Therefore, a major difference between the two approaches lies in the way the primary particles are treated: if the injected primary distributions are cooled by either synchrotron or inverse Compton radiation, this effect will be automatically included in AM^3, ATHEνA, and LeHaMoC, while B13 and LeHa-Paris need to parameterize the cooled primary distributions at equilibrium. In the case of cooling, the expression relating $n_i^{\rm ss}|_{\gamma=1}$ and the injection rate of primaries is given by (S. Inoue & F. Takahara 1996)

$$n_i^{\rm ss}|_{\gamma=1} = \gamma_c t_{i,\rm esc} e^{-\gamma_c} \int_1^\infty d\gamma Q_i^{\rm inj}(\gamma) e^{\gamma_c/\gamma}, \qquad (12)$$

where γ_c is the cooling Lorentz factor that is defined by balancing the radiative loss and escape timescales ($t_{i,\rm cool}(\gamma) = t_{i,\rm esc}$).

Another difference among the codes is the fact that LeHa-Paris and B13 implements the geometric correction described in R. J. Gould (1979) and J. Kataoka et al. (1999): the photon densities that are used for computing inverse Compton scattering and proton–photon interactions are multiplied by a factor of $3/4$ to account for the fact that the photon densities in one-zone codes are spatial averages; even if the emissivity of a process is isotropic in a spherical source, the photon densities are radially dependent (R. J. Gould 1979). This correction term is not implemented in the other codes, and in this work, the outputs from LeHa-Paris that are affected by this correction are multiplied by four-thirds at the plotting stage.

5. Results

We start by comparing the leptonic parts of our codes to gauge the level of agreement concerning the computation of synchrotron radiation and inverse Compton scattering (Section 5.1). We then investigated the agreement for the hadronic interactions in terms of secondary production spectra and their resulting emission (Section 5.3). The parameter values for all tests presented in this section are listed in Table 4.

5.1. Leptonic Scenarios

The first tests are done for a purely leptonic SSC scenario. We simulate emission for parameters typical of high-frequency-peaked BL Lacertae objects (see Table 4 for details). To investigate if there are any differences in the emissivity of the Compton scattering specific to the Thomson or the Klein–Nishina regime, we test for two different values of $\gamma_{e,\rm max} = 10^4$ (SSC-TH) and 10^6 (SSC-KN). For the adopted parameters, the steady-state electron distribution is uncooled, and Equation (11) is used for setting the initial conditions. The results of the modeling are provided in Figure 4, in which we show, for both tests, the SED output from the five codes, together with their average.[21] The subplots show the relative error of each model with respect to the average.

The leptonic simulations indicate that the shapes of the synchrotron and SSC components are well reproduced, and that the spread in normalization is within $\pm 10\%$ over a broad part of the SEDs. Larger deviations are seen at the cutoffs of each spectral component. For instance, differences in the low-energy cutoff of the synchrotron component can be traced back to different ways of computing the synchrotron self-absorption coefficient. By comparing the SSC-TH and SSC-KN simulations, we observe no significant differences in either spectral component.

We then compare the performance of time-dependent and steady-state codes for a case where radiative cooling is important. For power-law injections with slope $p \gtrsim 2$, the effect of synchrotron cooling, or inverse Compton cooling in the Thomson limit, is to create a break in the energy distribution; if the power-law distribution at injection is much harder ($p \ll 2$), then the particle distribution at equilibrium shows a pile-up instead. As an indicative example, we show a case where electrons cool due to synchrotron radiation (SYN-cool), and a cooling break is formed in their distribution. In Figure 5, we show, on the left panel, the electron distributions at equilibrium from ATHEνA and LeHaMoC, the corresponding analytical solution following Equation (12), and a simple broken power-law parameterization used in LeHa-Paris. Both solutions match in the power-law segment of the cooled distribution, but differ around the cooling break at $\gamma \sim 10$ and the high-energy cutoff; the parameterization used in LeHa-Paris produces a sharp cooling break that overestimates the steady-state electron distribution in that energy range. The difference in the high-energy cutoff of the electron distribution is mapped to the cutoff of the synchrotron spectrum. Because electrons with $\gamma \sim 10$ emit synchrotron photons at $\sim 10^{10}$ Hz (i.e., below the synchrotron self-absorption frequency), we do not directly observe in the synchrotron spectra the difference of the respective particle distributions at the cooling break. We also observe that the

[21] The average of νF_ν or $\gamma^2 dN/d\gamma dV$ is computed on a fixed grid on which the code outputs are interpolated.

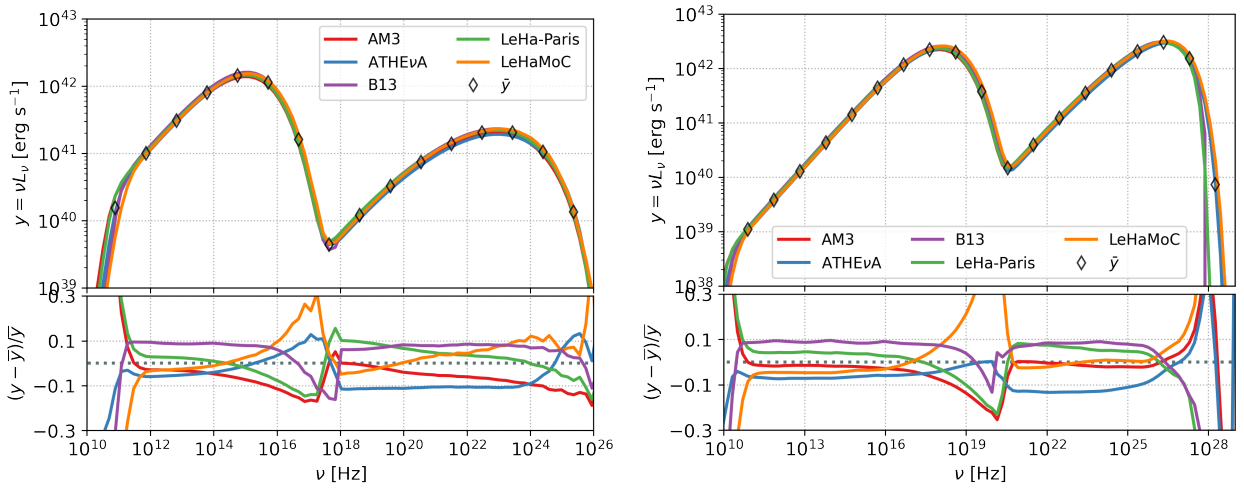

Figure 4. SEDs (in the observer's frame) computed for the SSC-TH (left) and SSC-KN (right) scenarios using the five codes described in Section 3 (see inset legend for details). The mean model is shown with open markers. The residuals of each code with respect to the mean value of the results are plotted in the bottom panels.

Table 4
Input Parameter Values Used for Each Scenario for the Code Comparison

		SYN-cool	SSC-TH	SSC-KN	pγ-MONOGB	pγ-PLPL	PS	LeHa
		Leptonic Scenarios			Hadronic Kernel Tests		Hadronic Blazar-like Scenarios	
Input Parameters	Symbol (Units)	Values						
Emission region radius	R [cm]	10^{15}	10^{15}	10^{15}	10^{15}	10^{15}	10^{15}	10^{16}
Magnetic field strength	B [G]	50	0.1	0.01	10		10	0.1
Min. e^- Lorentz factor	$\gamma_{e,\rm min}$	1	1	1	⋯	⋯	1	1
Max. e^- Lorentz factor	$\gamma_{e,\rm max}$	10^4	10^4	10^6	⋯	⋯	10^3	3×10^5
e^- power-law index	s_e	1.9	1.9	1.9	⋯	⋯	1.9	2.0
e^- injection luminosity[a]	$L_e^{\rm inj}$ [erg s^{-1}]	⋯	⋯	⋯	⋯	⋯	1.6×10^{38}	3.7×10^{40}
e^- injection compactness[b]	$\log(\ell_e^{\rm inj})$	−4.5	−4.47	−4.18	⋯	⋯	7.47	−5.1
Steady-state e density[c]	$n_e^{\rm ss}\vert_{\gamma=1}$ [cm^{-3}]	1.65×10^4	10^4	10^4	⋯	⋯	12.5	282
e^- escape timescale	$t_{e,\rm esc}$ $[R/c]$	1	1	1	⋯	⋯	1	1
Min. p Lorentz factor	$\gamma_{p,\rm min}$	⋯	⋯	⋯	$10^{6(7)}$	1	1	1
Max. p Lorentz factor	$\gamma_{p,\rm max}$	⋯	⋯	⋯	$10^{6.2(7.2)}$	10^8	10^8	10^7
p power-law index	s_p	⋯	⋯	⋯	1.9	1.9	1.9	2.0
p injection luminosity[a]	$L_p^{\rm inj}$ [erg s^{-1}]	⋯	⋯	⋯	8.5×10^{43}	8.5×10^{43}	10^{44}	2.8×10^{46}
p injection compactness[b]	$\log(\ell_p^{\rm inj})$	⋯	⋯	⋯	−4.0	−4.0	−4.93	−2.5
Steady-state p density[c]	$n_p^{\rm ss}$ [cm^{-3}]	⋯	⋯	⋯	$2.4(1.9)\times10^5$	8490	1000	108,300
p escape timescale	$t_{p,\rm esc}$ $[R/c]$	⋯	⋯	⋯	1	1	1	1

Notes.
[a] AM^3 and LeHaMoC.
[b] ATHEνA.
[c] LeHa-Paris and B13. Particle cooling neglected in SSC-TH, SSC-KN, pγ-MONOGB, pγ-PLPL, and γγ-annihilation was omitted in PS. pγ-MONOGB: graybody external photon field of compactness $\ell_\gamma = 8.1\times10^{-6}$ and temperature $T_\gamma = 10^6$ K. pγ-PLPL: power-law external field of compactness $\ell_\gamma = 10^{-5}$ between $E_{\gamma,\rm min} = 10^{-6} m_e c^2$ and $E_{\gamma,\rm max} = 10^{-1} m_e c^2$, with power-law index $p_\gamma = 2.0$. A Doppler factor of 30 was used to transform the luminosities from the jet comoving frame to the observer's frame.

synchrotron self-absorption computed with LeHaMoC is higher by a factor of 4 compared to the other codes. As pointed out in S. I. Stathopoulos et al. (2024b) such differences can be attributed to the method of computing the self-absorption coefficient. For example, if we use in LeHaMoC the δ-function approximation for the particle emissivity in the calculation of the absorption coefficient as done in ATHEνA, the ratio between LeHaMoC and ATHEνA is less than ∼1.5 in the self-absorbed part of the spectrum, as shown in Section 3.2.1 in S. I. Stathopoulos et al. (2024b).

5.2. Hadronic Scenarios: Kernel Test Cases

After investigating the differences in the leptonic modules of the codes, we can compare the implementation of hadronic

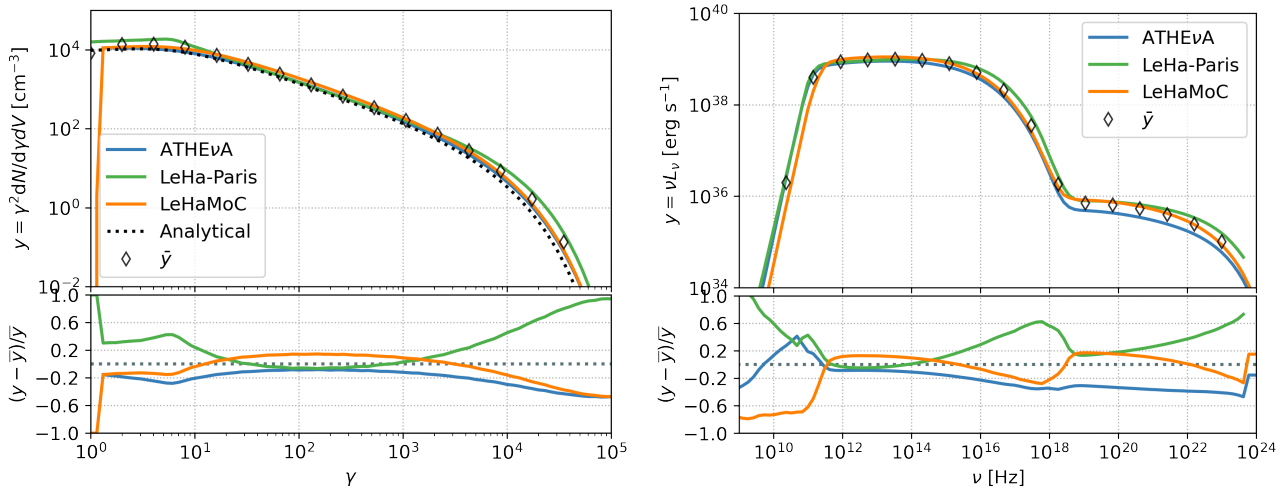

Figure 5. Steady-state electron distribution (left) and SSC spectra in the jet comoving frame (right) computed for the SYN-cool case using three of the codes described in Section 3. Dotted line on the left panel shows the analytical steady-state electron distribution (S. Inoue & F. Takahara 1996).

interactions. To better identify potential discrepancies, we study first the injection spectra of secondary particles produced in interactions of protons with nonevolving (fixed) photon distributions. The purpose of this comparison is to test the implementation of the conventional kernel functions for the production spectra of secondaries.

We start by studying proton–photon interactions between monoenergetic[22] protons and photons following a graybody distribution.[23] We choose protons with $\gamma_p = 10^6$ and a graybody photon distribution of temperature $T_\gamma = 10^6$ K and compactness $\ell_\gamma = 8.1 \times 10^{-5}$; this is a dimensionless measure of the radiation energy density u_γ and is defined as $\ell_\gamma = u_\gamma \sigma_T R/(3 m_e c^2)$. For the adopted parameters, photo-meson interactions of protons with photons from the peak of the graybody distribution, $\epsilon_{pk} \sim 3 k_B T$, happen close to the Δ^+ resonance. Due to a much lower energy threshold for Bethe–Heitler interactions ($\sim m_e/m_\pi$), the selected parameters lead to far from threshold Bethe–Heitler interactions. These are characterized by broad (almost flat) energy injection spectra (D. Karavola & M. Petropoulou 2024).

The results of this test (pγ-MONOGB) are shown in Figure 6, in which we provide the energy injection spectra for photons from π^0 decay, leptons from $\pi^\pm$ decay, and leptons from Bethe–Heitler pair production.[24] When comparing ATHEνA, LeHa-Paris, and B13 we find that the pionic gamma-ray spectra and all-flavor neutrino spectra agree within $\pm 20\%$ over a large part of the spectrum, with divergence only at cutoffs. The difference grows to $\pm 30\%$ when considering the leptonic production spectra for a wide range of particle energies. We observe here that especially AM^3 exhibits a very different behavior from the other cases. This is not unexpected: its photohadronic interaction module is based on S. Hummer et al. (2010), which was optimized for power-law spectra balancing performance and precision. More concretely, the results are based on efficient single integrations by discretizing the integral over the secondary redistribution functions (based on different physics processes)—instead of using the usual Green's function/kernel approach. This yields unwanted spikes and features if quasi-monochromatic protons or target photons (or sharp cutoffs) are used, see also Figure 9 in S. Hummer et al. (2010). An updated approach has been published in D. Biehl et al. (2018; Appendix A.3), where the discretization is automatized, and the center-of-mass energy dependency of the redistribution functions (leading to even stronger discrepancies at higher energies, see Appendix B.2) is improved—at the expense of losing the relationship to the underlying physics processes. It is useful to inspect Figure 23 (upper right panel) of that article: the total spectrum is composed of different spectra added together with different values of the secondary to primary energy ratio (instead of integrating over it). Omitting certain contributions of that parameter leads to an under-prediction of the secondary spectrum in certain ranges, which can also be seen at low and high energies in Figure 6. The original approach in S. Hummer et al. (2010) compensates for this partially by choosing larger multiplicities, which leads to the sharp features.

The agreement for the Bethe–Heitler injection is considerably better than the photo-meson part at the flat part of the spectrum, well within $\pm 15\%$, for three of the codes. ATHEνA overestimates the Bethe–Heitler injection at all energies: this behavior is understood as an effect of the fixed energy grid resolution in the code that is not optimized for very narrow proton distributions; in Appendix C, we provide more details about this aspect and show that the agreement is recovered when the proton distribution is widened.

We then consider the case of interacting power-law protons with power-law photon distributions, which can be of more general applicability to astrophysical systems. For the adopted parameters (see pγ-PLPL in Table 4), the energy of the proton distribution is carried by the most energetic particles of the distribution with $\gamma_{p,\max} = 10^8$. Therefore, the secondary spectra will be determined by the interactions of the most energetic protons of the power law. These protons will interact just above the pion production energy threshold $\bar{\epsilon}_{\mathrm{th,p}\gamma} \simeq 0.145$ GeV, with the lowest energy photons from the power law, which are the most numerous since $E_\gamma dN/dE_\gamma \propto E_\gamma^{-1}$. Due to the lower

[22] A truly monoenergetic distribution cannot be implemented in codes that are expecting as input parameters the minimum/maximum energy of the particle distribution and the spectral index. A monoenergetic distribution is therefore approximated by the narrowest boxlike energy distribution allowed by the grid resolution.

[23] A radiation field with a spectrum following the Planck function of temperature T, but with a total energy density smaller than $u_{\mathrm{BB}} = aT^4$.

[24] Results for a higher proton energy are provided in Appendix B.2.

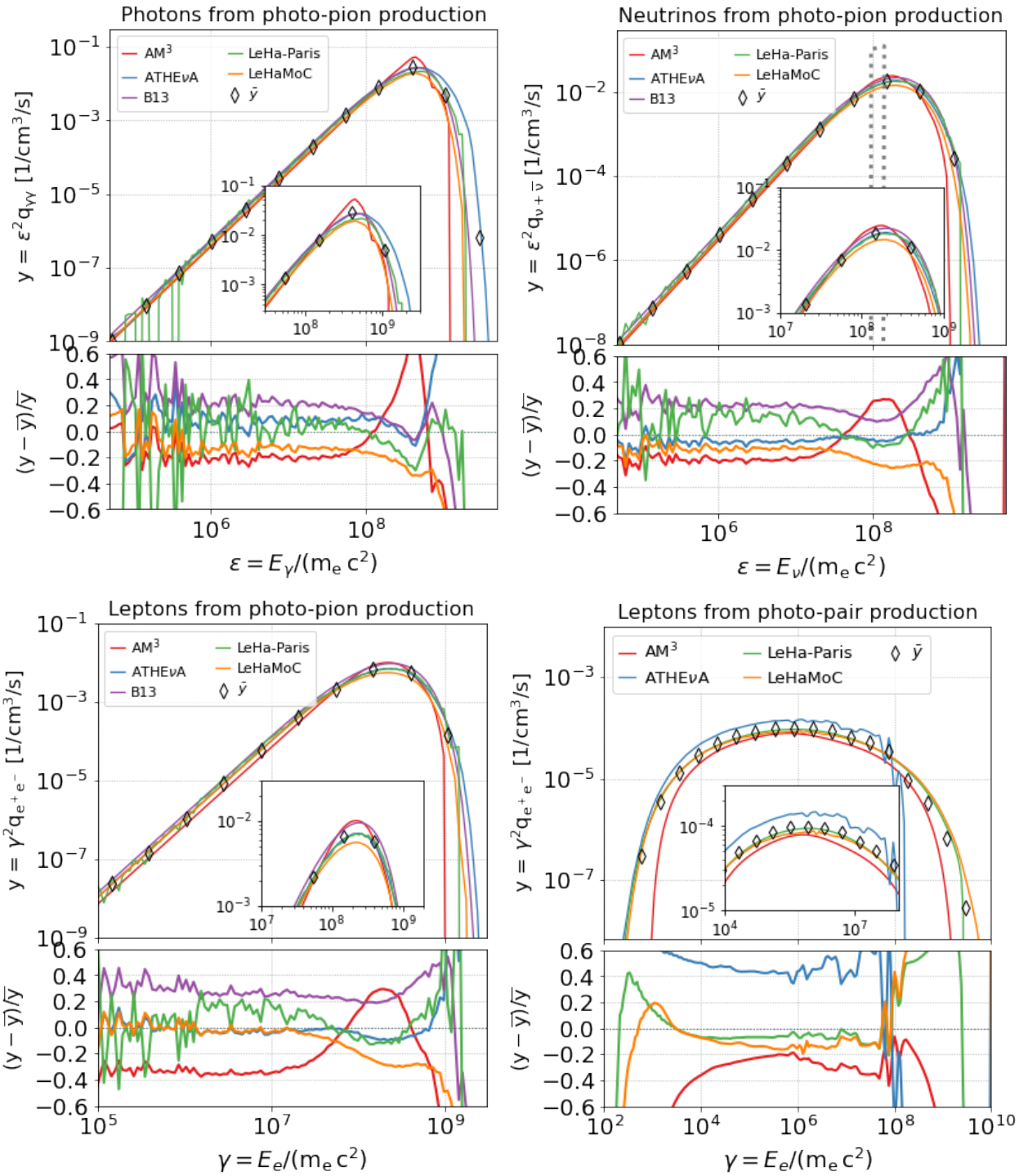

Figure 6. Production rates per unit volume of secondaries (photons, leptons, and neutrinos of all flavors) from photo-pion production and photo-pair production for the case of a quasi-monoenergetic proton distribution with $\gamma_p = 10^6$ interacting with a graybody radiation field (see pγ-MONOGB in Table 4). Inset panels show a zoom into the energy range around the peak of the curves. The residuals of each code with respect to the mean value of the results are plotted in the bottom panels. The dotted gray line in the top right panel shows the analytical neutrino spectrum computed as explained in Appendix A.

energy threshold of the Bethe–Heitler pair production process, $\bar{\epsilon}_{\rm th,BH} \simeq 1$ MeV, the most energetic protons will interact far from the threshold with the lowest energy photons of the power-law distribution.

The results for the pγ-PLPL are presented in Figure 7. Inspection of the gamma-ray, lepton, and neutrino spectra from pion decays shows that the differences between codes are between ±30% and ±40% for the different species. The spectral shapes are similar around and below the peaks, with differences becoming larger at the cutoffs. The ordering of codes in terms of their relative difference with respect to the mean is the same for all particle species. At first thought the larger differences found here compared to the pγ-MONOGB cases may seem unexpected. However, in Appendix B, we

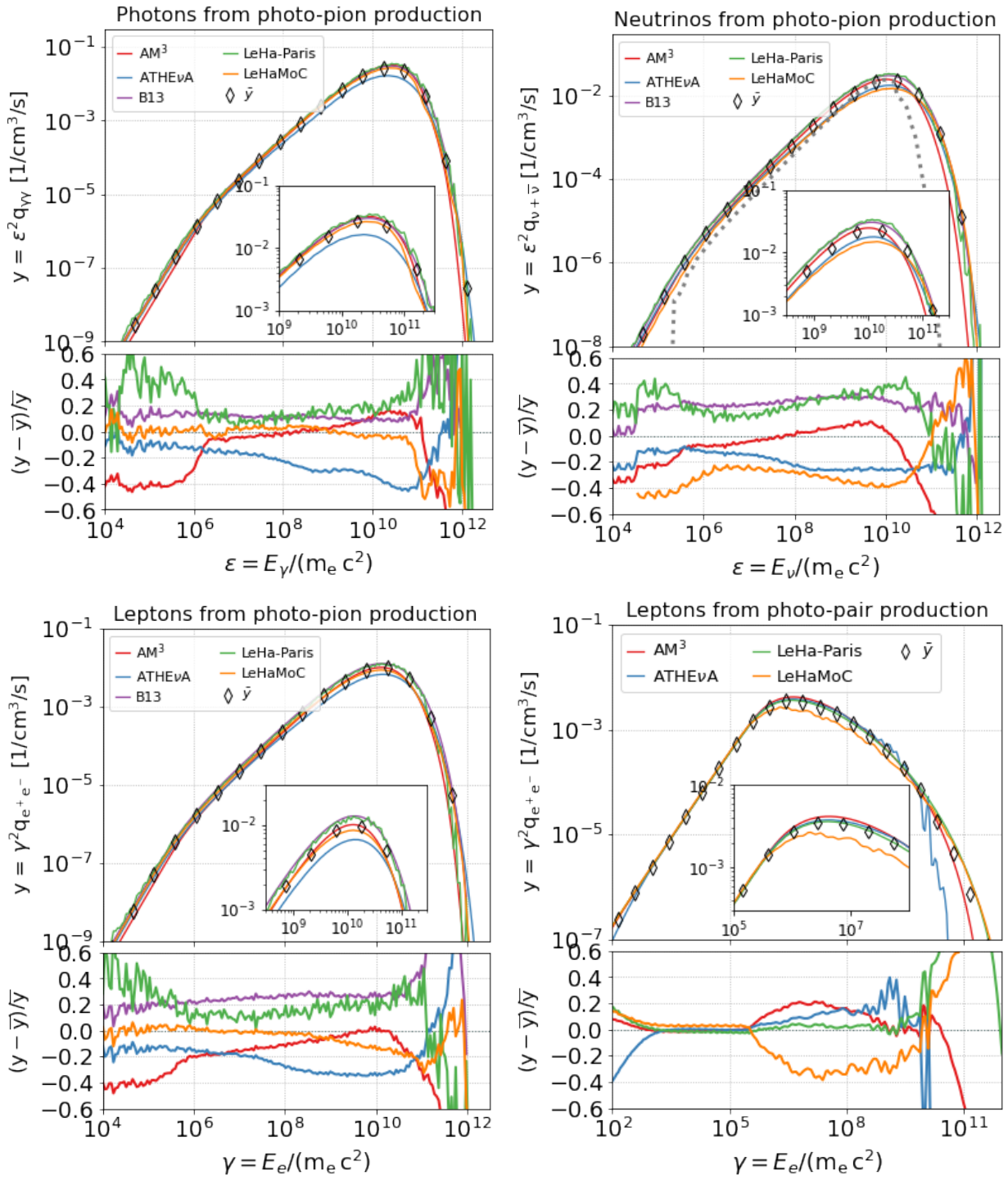

Figure 7. Same as in Figure 6 but for the case of a power-law proton distribution interacting with a power-law radiation field (see pγ-PLPL in Table 4). The dotted gray line in the top right panel shows the analytical neutrino spectrum computed as explained in Appendix A.

show that even in the pγ-MONOGB cases, the relative differences increase up to ±40% as the typical interaction energy increases (compare Figures 6 and 16). Therefore, by summing up the contributions from near and far from threshold interactions, such differences tend to accumulate. The maximum relative difference will depend on the power-law slopes and the energy limits of both distributions, as these variables determine essentially the relative contribution of far and near-threshold interactions to the total spectrum. Interestingly, the differences in the pair production spectra are much smaller, less than 20% at the peak energy. Contrary to the broad and almost flat pair production energy spectra computed for the pγ-MONOGB cases, the spectra exhibit a clear peak at $\gamma \sim 10^6$, which is relatively narrow. These spectral properties suggest that the maximum energy injection rate is determined by near-threshold interactions of protons with $\gamma_p = 10^6$ with the lowest energy photons of the power law (for more details, see D. Karavola & M. Petropoulou 2024). It is interesting to note that for AM^3, the earlier found seemingly large discrepancies in the photo-meson injection with respect to

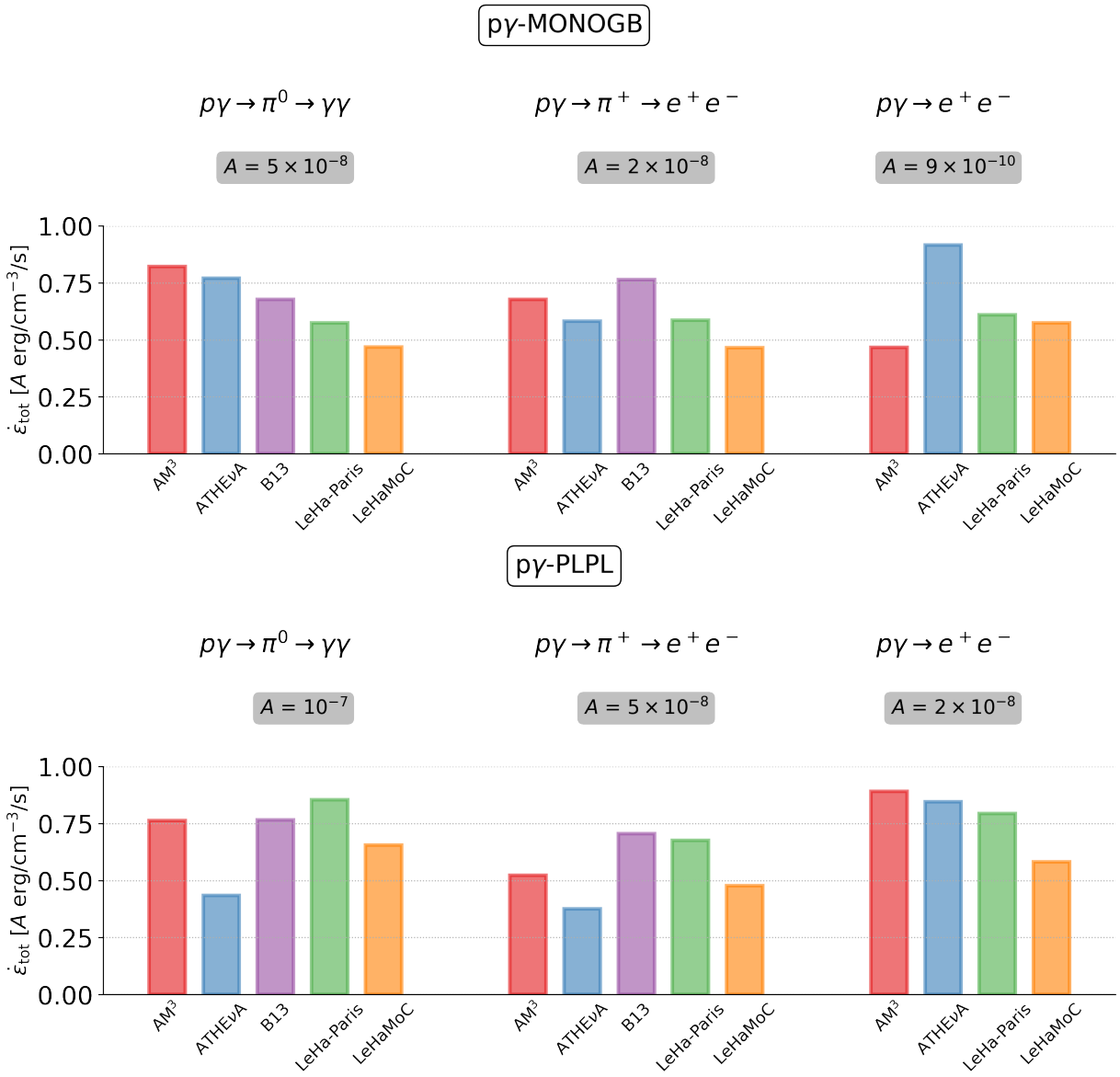

Figure 8. Integrated energy density injection rates of secondaries from neutral pion decay, charged pion decay, and photo-pair production computed for proton interactions with a graybody radiation field for $\log_{10}(\gamma_p) = 6$ (top) and a power-law proton distribution interacting with a power-law radiation field (bottom). To infer the actual energy injection rate, the height of each bar should be multiplied by the appropriate normalization factor A.

the mean model disappear close to the peaks, and the spectra almost match perfectly with the other codes, which comes from the aforementioned optimization for power-law spectra.

We additionally compare the volumetric energy injection rates of the five codes by integrating the differential production spectra (per unit volume) over the photon energies and lepton Lorentz factors. The results are displayed in Figure 8 in the form of bar charts. Because the energy injection spectra of all particle species produced in photo-meson interactions have a well-defined peak, the differences displayed around the maximal values in the differential energy spectra are also reflected in the differences shown in the bar charts.

5.3. Hadronic Blazar-like Scenarios

We now investigate the agreement among codes for more *blazar-like* cases, and we study in particular two emission scenarios that have been put forward to explain blazar SEDs: the first one is a proton synchrotron (PS) solution, in which the high-energy SED peak is ascribed to synchrotron emission by primary protons in the emitting region, and in which the emission by secondary particles produced in proton–photon interactions emerges only at higher energies, and is sub-dominant with respect to the proton synchrotron one; the second one is a hybrid, leptohadronic (LeHa) solution, in which the high-energy SED component is due to both primary electrons (via SSC) and radiation by secondary leptons produced in proton–photon interactions. With respect to the previous tests, there are no external photon fields, and the proton–photon interactions happen (mainly) between primary protons and synchrotron photons by primary electrons. For both tests, we are now interested in comparing the multi-messenger photon/neutrino SEDs (in luminosity, $\nu L(\nu)$), and the injection rates are not shown. We only show here the results from the four codes that include the Bethe–Heitler process.

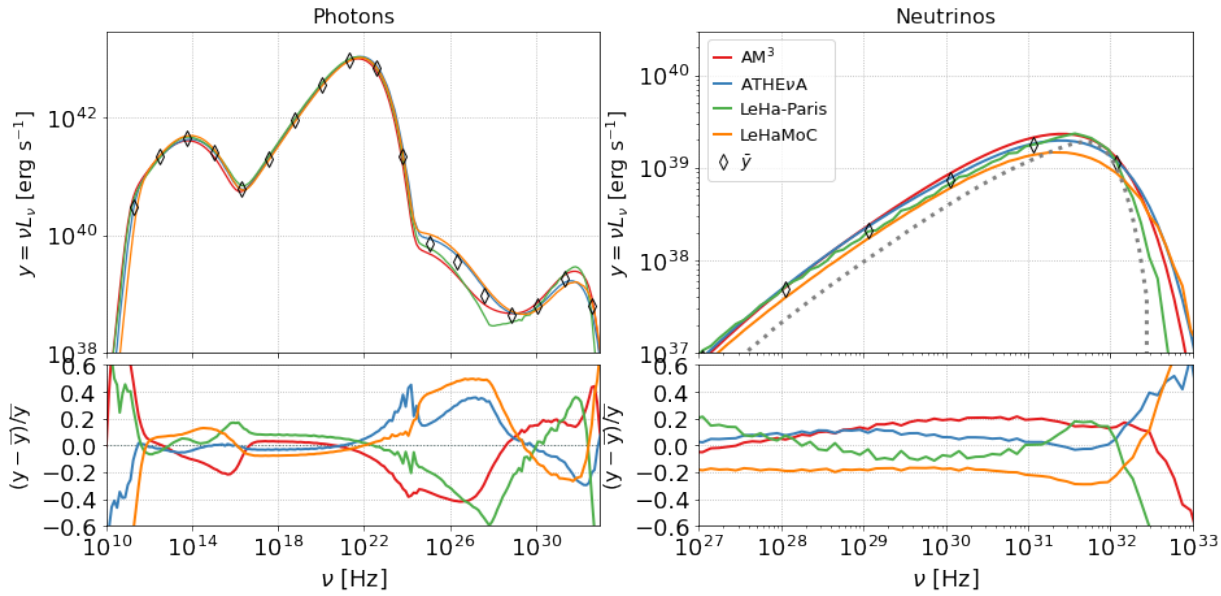

Figure 9. SEDs (in the observer's frame) of photons and neutrinos (of all flavors) computed for the PS scenario (see Table 4). The mean model is shown with open markers. The residuals of each code with respect to the mean value of the results are plotted in the bottom panels. The dotted gray line in the top right panel shows the analytical neutrino spectrum computed as explained in Appendix A.

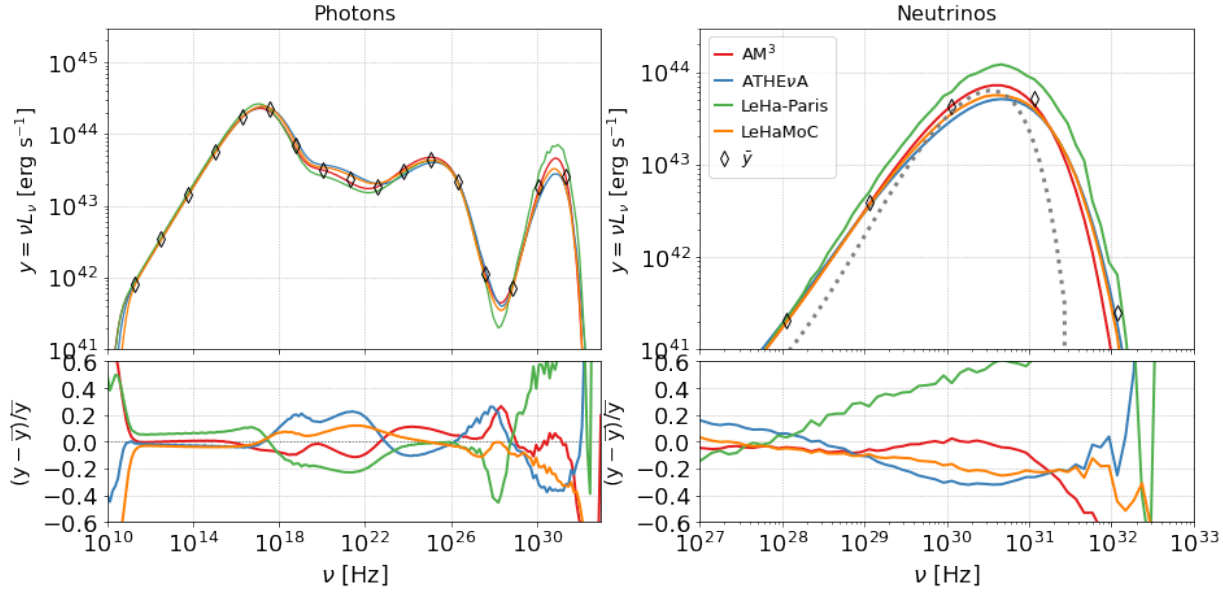

Figure 10. Same as in Figure 9 but for the LeHa scenario (see Table 4).

The proton synchrotron test has the same proton distribution as the previous test ($p\gamma$-PLPL), i.e., a power-law proton distribution between $\gamma_{\rm p,min} = 1$ and $\gamma_{\rm p,max} = 10^8$ and index of 1.9; in the leptohadronic test, in order to get an SED more typical of a blazar, we adopt a softer index (2.0) and lower maximum proton Lorentz factor (10^7). The details of the model parameters are provided in Table 4, and the multi-messenger SEDs are shown in Figure 9 (for the PS test) and Figure 10 (for the LeHa test).

The proton synchrotron SED shows four distinct components in order of increasing energy: synchrotron by primary electrons, synchrotron by primary protons, synchrotron by Bethe–Heitler pairs, and photons from π^0 decay. To ease the comparison and the identification of the various processes, $\gamma - \gamma$ absorption is turned off for this test only. As can be seen from Figure 9, the photon SEDs agree at the level of ±15% in the energy ranges where electron and proton synchrotron emission dominate. The differences among the codes increase to about ∼20% at the highest energies, where the π^0 bump emerges. The largest difference (±40%) is found at energies where the synchrotron emission from Bethe–Heitler pairs dominates. For the neutrino spectrum, we also show the result from a semianalytical calculation described in Appendix A. While the semianalytical result captures the peak of the neutrino SED well, it produces a narrower spectrum overall, because it assumes a one-to-one mapping between the energies of the parent proton and the produced neutrino (see Equation (A3)). In other words, the semianalytical approach does not account for the spread in neutrino energies produced by a single proton.

The leptohadronic SEDs also show four components in order of increasing energy: synchrotron by primary electrons, synchrotron by Bethe–Heitler pairs, a superposition of SSC and synchrotron by photo-meson pairs, and photons from π^0 decay. As can be seen from Figure 10, the photon SEDs show a remarkable agreement within $\pm 20\%$, with the exception of the π^0 component that opens up to -40%–60%. The same larger spread can be seen in the neutrino spectra that show -30% to 60%. The dispersion is driven by the LeHa-Paris result that overestimates the others. It is not completely clear why this particular test shows a larger spread in the photo-meson injection: part of it could be related to the fact that with these model parameters the primary electrons are cooled, and LeHa-Paris parameterizes primary particles with a broken power-law function (see Section 5.1 and Figure 5); the overestimation by about 15% of the peak of the electron synchrotron implies a larger target density for photo-meson interactions and thus a brighter neutrino emission by the same amount. Finally, the neutrino spectrum from the semianalytical approach matches the peak of the neutrino SEDs computed with AM^3, ATHEνA, and LeHaMoC, but produces a narrower spectrum.

6. Other Scenarios

In this section, we test the performance of the time-dependent codes AM^3 and ATHEνA in computing the spectral and temporal behavior of high-density emitting regions, using a leptonic (Section 6.1) and purely hadronic scenario (Section 6.2). While these test cases have not been directly applied to AGN modeling, they are ideal for highlighting the nonlinear coupling among different particle species. The physical parameters used in these tests are provided in Table 5.

Table 5
Parameters for the Other Scenarios

Inverse Compton Catastrophe		PPS Loop	
Parameter	Value	Parameter	Value
B [G]	10	B [G]	31.6
R [cm]	10^{16}	R [cm]	10^{15}
$\gamma_{e,\min}$	$10^{1.9}$	$\gamma_{p,\min}$	$10^{0.1}$
$\gamma_{e,\max}$	$10^{2.1}$	$\gamma_{p,\max}$	10^{5}
p_e	2.0	p_p	2.0
log (ℓ_e)	0.0	log (ℓ_p)	$\{-3.2, -2.9, -2.6, -2.3\}$
$t_{e,\mathrm{esc}}$ $[R/c]$	1	$t_{p,\mathrm{esc}}$ $[R/c]$	10^3

Note. Inverse Compton catastrophe: synchrotron self-absorption and $\gamma\gamma$-annihilation were not taken into account. PPS loop: synchrotron self-absorption, leptonic and hadronic inverse Compton, photo-pion production, and $\gamma\gamma$-annihilation were not taken into account.

6.1. Nonlinear Electron Cooling: The Case of Inverse Compton Catastrophe

The term "inverse Compton catastrophe" refers to the dramatic rise in the luminosity of inverse Compton–scattered photons that would occur due to the rapid cooling of electrons via inverse Compton scattering (M. S. Longair 2011).

In a synchrotron-emitting source Compton catastrophe can be realized when the energy density of the magnetic field, which determines the rate of electron cooling through synchrotron radiation, is much lower than the energy density of synchrotron photons. A runaway process is therefore possible to develop: low-energy (e.g., radio) photons produced by synchrotron radiation are scattered to higher energies (e.g., in X-rays) by the same relativistic electron population. If the energy density of these high-energy photons is larger than that of synchrotron photons, the electrons would suffer even greater energy losses by upscattering them to even higher energies, e.g., in gamma rays. These photons would have, in turn, greater energy density than the X-ray photons, and so on. This process would eventually cease when the highest order inverse Compton scatterings would take place in the Klein–Nishina regime (e.g., M. Petropoulou et al. 2015b).

Here, we compare two of the codes (AM^3 and ATHEνA) that can treat nonlinear cooling of the electron population. For this purpose, we use parameters that lead the source into the Compton catastrophe regime, namely, $B = 10\,\mathrm{G}$, $R = 10^{16}\,\mathrm{cm}$, $\ell_e^{\mathrm{inj}} = 1$ or $L_e^{\mathrm{inj}} = 4.6 \times 10^{45}\,\mathrm{erg\ s^{-1}}$ (see Equations (8) and (9)), $s_e = 2$, $\gamma_{e,\min} = 10^{1.9}$, and $\gamma_{e,\max} = 10^{2.1}$; an exponential cutoff at $\gamma_{e,\max}$ was also used.

For the selected parameters, electrons are fast cooling, as indicated by the extension of the electron distribution to $\gamma_e \ll \gamma_{e,\min}$ within one dynamical timescale (see left top panel in Figure 11). Differences in the shape of the electron distribution at $\gamma_e < 2$ are mainly caused by differences in the energy grid resolution of the two codes, the default choice for ATHEνA being 10 points per decade in energy compared to 20 points per decade used in AM^3. We refer the reader to Section 3.6 for details on the impact of the energy grid and temporal resolution used in the two codes. Moreover, there is a good agreement between the codes in terms of the total energy carried by the electron distribution over the course of 10 dynamical times, as shown in the bottom left panel of Figure 11. Finally, the broadband photon spectra are displayed in the right panel of the figure (top) with the relative difference also shown in the bottom panel. Despite the nonlinearity of the physics problem at hand, the two codes predict fluxes that differ at most by 10%, similarly to the SSC model presented in Figure 4.

6.2. Nonlinear Proton Cooling: The Pair Production/Synchrotron Loop

Relativistic protons can, under certain conditions, participate in various types of radiative instabilities (see A. Mastichiadis et al. 2020, for a comprehensive study). When the proton energy density in the source exceeds some critical value, a runaway process is initiated, resulting in the explosive transfer of the proton energy into electron–positron pairs, radiation, and neutrinos. The runaway also leads to an increase in the radiative efficiency (defined as the ratio of the photon luminosity to the injected proton luminosity).

One of these hadronic radiative instabilities, known as the pair production/synchrotron (PPS) loop, was first studied by J. G. Kirk & A. Mastichiadis (1992). We consider a source containing relativistic protons and magnetic fields (hence, this is a purely hadronic scenario). If the conditions (i.e., magnetic field strength and proton Lorentz factor) are such that the pairs produced by photo-pair production radiate synchrotron photons that are also targets for photo-pair production, a closed loop of physical processes is formed. This loop can be self-sustained if at least one of the synchrotron photons

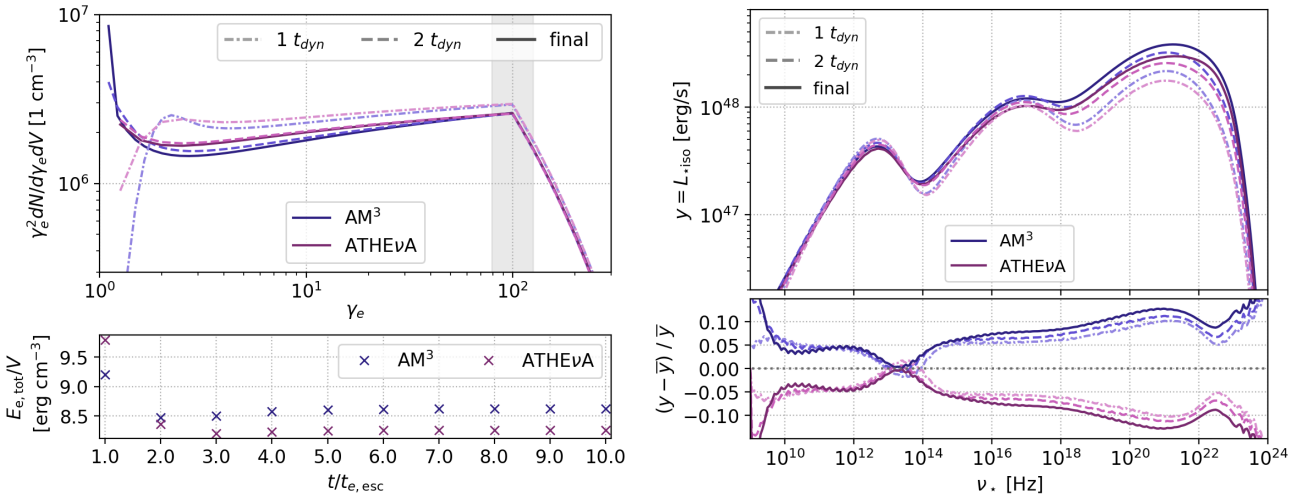

Figure 11. Results for an inverse Compton catastrophe scenario computed using AM^3 and ATHEνA. Left panel: electron energy distributions. Thick solid lines show the steady-state distributions, while thin dashed–dotted and dashed lines show the distributions after one and two dynamical times, respectively. The gray-shaded region indicates the energy range of injected electrons. The bottom panel shows the temporal evolution of the electron energy density. Right panel: photon SEDs for the same time stamps shown on the left panel. Residuals with respect to the mean are shown in the bottom panel.

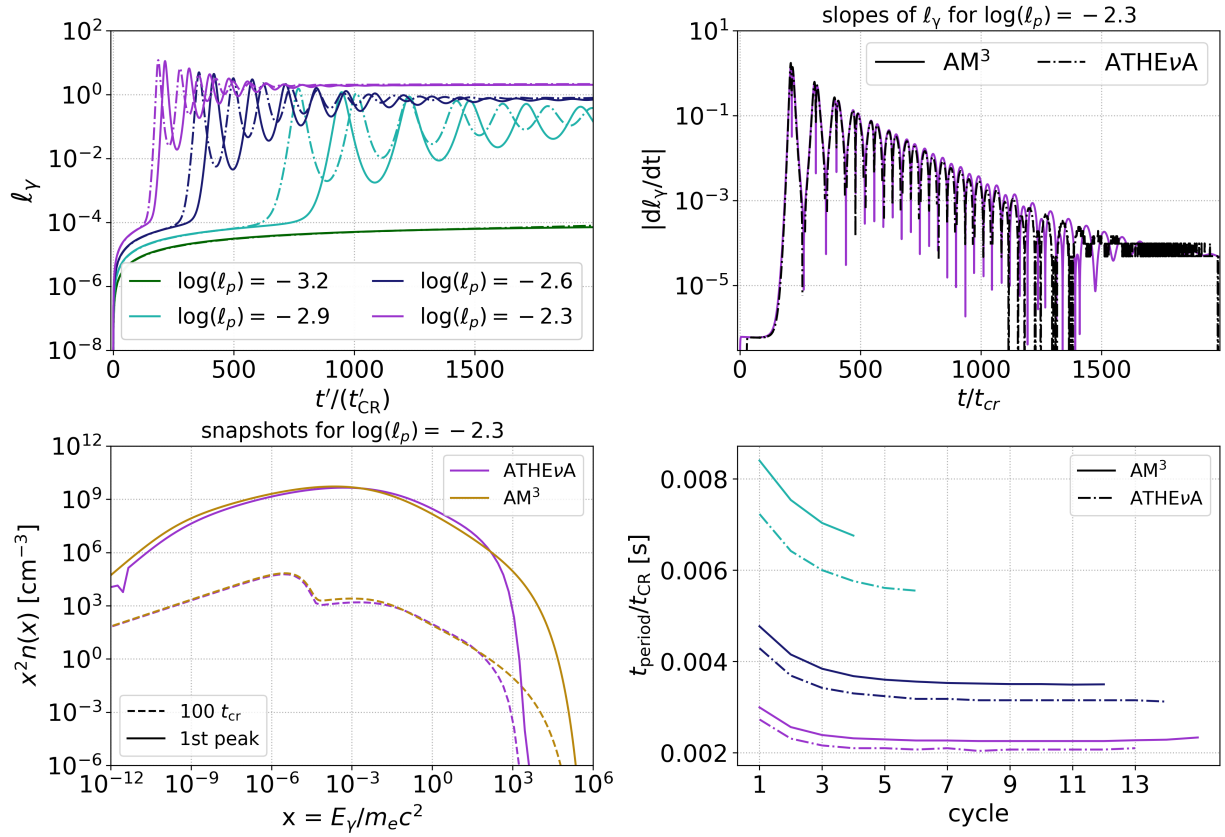

Figure 12. Results for the PPS scenario computed using AM^3 and ATHEνA. From top left and in clockwise order we show (i) time series of the photon compactness ℓ_γ (i.e., dimensionless light curves) computed for four values of the proton injection compactness ℓ_p (see inset legend), (ii) time derivative of the light curve computed for the highest value of ℓ_p (after applying a shift to the light curves to make them overlap), (iii) two snapshots of the photon spectra for the highest value of ℓ_p, and (iv) evolution of the period with the number of cycles for the three light curves in the first panel exhibiting damped oscillatory behavior (same color coding used).

produces a pair before escaping the source. This condition translates to a critical proton density (see Equation (2) in J. G. Kirk & A. Mastichiadis 1992), which whenever surpassed, leads to an explosive transfer of proton energy to photons.

While the growth rate of the instability can be computed semianalytically (J. G. Kirk & A. Mastichiadis 1992), a study of the instability in the nonlinear regime requires a full numerical treatment (A. Mastichiadis et al. 2005, 2020). The PPS loop is therefore an excellent case study for comparing the

performance of the two time-dependent codes AM^3 and ATHEνA.

An illustrative example of the PPS loop is presented in Figure 12 for $B = 10^{1.5}$ G, $R = 10^{15}$ cm, and $t_{p,\rm esc} = 10^3\, R/c$. The top left panel shows the bolometric photon compactness as a function of time computed for different proton compactnesses, ranging from $10^{-3.2}$ (green curves) to $10^{-2.3}$ (purple curves) with logarithmic increments of 0.3. For proton densities below a critical value, the system reaches a steady state that corresponds to a constant photon compactness (green curves). Above the critical proton density, however, nonlinear feedback between protons and synchrotron photons from Bethe–Heitler pairs becomes relevant, and the photon light curve exhibits outbursts that correspond to times of efficient proton cooling. Both numerical codes can capture the transition from the linear to the nonlinear regime (green and cyan lines) for the same ℓ_p values, as well as the damped oscillatory behavior of the proton–photon system that was first presented in (A. Mastichiadis et al. 2005). This is the first time that the oscillations can be reproduced with a code other than ATHEνA.

There is a constant offset between the peak times of the outbursts, whose origin could not be pinned down. Similar offsets have been observed in numerical runs performed with ATHEνA, after changing, for example, the difference scheme used to replace the partial derivatives. Regardless, we find an excellent agreement between the codes in terms of period and period evolution (see the lower right panel). In the top right panel, we also show the time derivative of the light curve as a function of time, after correcting for the offset. There is very good agreement between the codes in describing the shape of the light curve. Finally, the broadband photon spectra computed at two indicative times (at the onset of the instability, and at the peak time of the first outburst) are presented in the bottom left panel of the same figure. There is good agreement in terms of shape and normalization. The difference in the high-energy cutoff of the synchrotron spectra is to be expected, since the pair injection spectra in ATHEνA cut off abruptly (see also Figure 6).

7. Summary and Conclusions

We have presented the results from the first comparison among five hadronic codes developed to model photon and neutrino emission from blazars. We started by comparing the leptonic part of the codes (synchrotron and SSC), showing that we have a general agreement at the level of $\pm 10\%$. The hadronic part is first checked by looking at tests for monoenergetic/power-law proton distributions interacting with simple photon fields (graybody or power law). In these cases, we are interested in comparing the injection rates of secondary particles produced in p-γ interactions. The level of agreement is at the level of $\pm 20\%$ to $\pm 40\%$. It is more difficult here to provide a simple value, as the dispersion depends on the specific test, the process we are evaluating, and the energies (with large deviations observed at cutoffs). A $\pm 40\%$ systematic spread represents a conservative value for the typical largest envelop we observe (excluding the cutoffs where anyhow the flux is fast dropping). The final comparisons are performed on two realistic, blazar-like tests in which we show the agreement in terms of photon and neutrino SED. In these two cases, as well the agreement ranges from $\pm 20\%$ to $\pm 40\%$. It is again difficult to gauge what will be the systematic uncertainty for another test performed elsewhere in the parameter space to model a future gamma–neutrino source, but we consider that $\pm 40\%$ can be considered a conservative, energy-independent, value to be adopted when comparing a single realization from a single code to observations.

Some important caveats should be highlighted here. The code comparison presented here has been done by putting all codes in the same conditions, to isolate only the differences coming from the implementation of hadronic processes. There are other assumptions and hypotheses in the numerical codes that have an impact on the overall normalization, and thus add up to the spread quantified here. The most relevant for this study is the correction for the radial dependency of the photon distribution in a sphere, which contributes an extra 25%. In a similar way, the hypothesis on the equilibrium distribution of primary electrons also impacts the photon output, and not just in a direct way by modifying their synchrotron emission, but also indirectly by changing the target photon field for p-γ interactions. In addition, in some part of the parameter space, some processes that are included in some codes but not in others become relevant if not dominant (i.e., Bethe–Heitler pair production, or synchrotron by muons), and this aspect should be carefully checked when exploring a large parameter space. In an effort to facilitate reproducibility and to benchmark any future code development in the community (that already happened since the TXS 0506+056 event and while this comparison project was in preparation, see, e.g., B. Jiménez Fernández & H. van Eerten 2021; S. Gasparyan et al. 2022; M. Zacharias et al. 2022), we release all output files from all codes used to produce the comparison plots in this paper as online material at doi:10.5281/zenodo.17177642.

Acknowledgments

M.P. and S.D. acknowledge support from the Hellenic Foundation for Research and Innovation (H.F.R.I.) under the "2nd call for H.F.R.I. Research Projects to support Faculty members and Researchers" through the project UNTRAPHOB (Project ID 3013). X.R. was supported by the Deutsche Forschungsgemeinschaft (DFG, German Research Foundation) through grant SFB 1258 "Neutrinos and Dark Matter in Astro- and Particle Physics" and by the Excellence Cluster ORIGINS, which is funded by the DFG under Germany's Excellence Strategy—EXC 2094—390783311.

Appendix A
Semianalytical Calculation of Neutrino Spectra

Throughout the paper, we compare the neutrino fluxes obtained with the five numerical codes to the neutrino fluxes obtained with a simple semianalytical calculation in order to test the range of applicability of this method, which is frequently employed in the literature.

The photo-meson production timescale for protons with Lorentz factor γ_p interacting with an isotropic photon distribution with differential number density $n_{\rm ph}(\epsilon)$ is defined as (F. W. Stecker 1979)

$$t_{\rm p\gamma}^{-1}(\gamma_p) = \frac{c}{2\gamma_p^2}\int_{\epsilon_{\rm th}}^{\infty} d\epsilon_\gamma\, \sigma_{\rm p\gamma}(\epsilon_\gamma)\,\kappa_{\rm p\gamma}(\epsilon_\gamma)\,\epsilon_\gamma \times \int_{\epsilon_\gamma/(2\gamma_p)}^{\infty} d\epsilon \epsilon^{-2} n_{\rm ph}(\epsilon), \quad \text{(A1)}$$

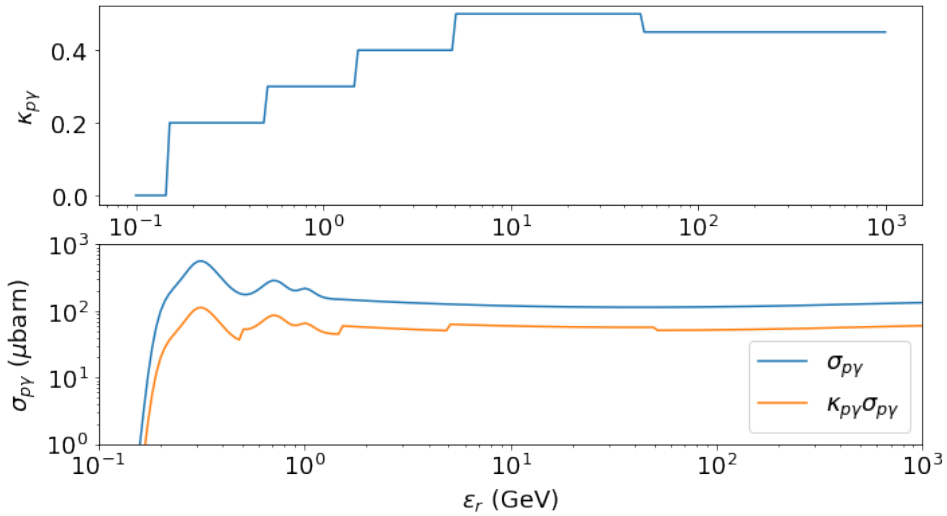

Figure 13. Parameterization of the inelasticity (top panel) and the cross section (bottom panel) for photo-meson production obtained from GEANT4 as a function of the interaction energy (K. Murase & S. Nagataki 2006).

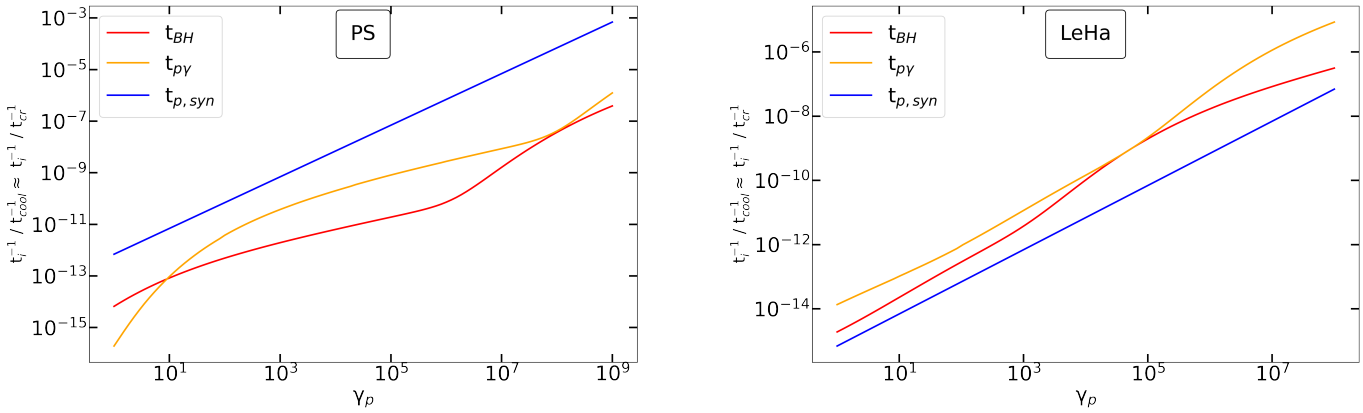

Figure 14. Normalized proton loss rates for the PS and LeHa scenarios. In both cases, the Bethe–Heitler, photo-meson, and proton synchrotron loss rates are much smaller than the proton escape rate, hence $t_{\rm cool} \approx t_{\rm cross}$.

where ϵ_γ is the photon energy in the proton rest frame, $\epsilon_{\rm th} \sim 145$ MeV is the threshold energy for pion production, and $\sigma_{\rm p\gamma}$ and $\kappa_{\rm p\gamma}$ are the cross section and inelasticity of photo-meson interactions, respectively. For $\sigma_{\rm p\gamma}$ and $\kappa_{p\gamma}$, we use a fit to the energy-dependent cross section and a multistep parameterization of the inelasticity (shown in Figure 13) obtained by running GEANT 4 (see also K. Murase & S. Nagataki 2006).

In general, the fraction of energy converted to pions is estimated as, $f_{\rm p\gamma} \equiv t_{\rm cool}/t_{\rm p\gamma}$, where $t_{\rm cool}$ is the proton energy loss cooling time, defined as

$$t_{\rm cool}^{-1} \equiv t_{\rm cross}^{-1} + t_{p,\rm syn}^{-1} + t_{\rm p\gamma}^{-1} + t_{\rm BH}^{-1}, \tag{A2}$$

where the synchrotron cooling time for protons with energy ε_p in a magnetic field with strength B is given by $t_{p,\rm syn} = 6\pi m_p^4 c^3/(m_e^2 \sigma_T B^2 \varepsilon_p)$.

The crossing time, $t_{\rm cross} = r_b/c$, approximates the adiabatic energy loss rate. The Bethe–Heitler energy loss timescale, $t_{\rm BH}$, is calculated as described in Appendix A of S. I. Stathopoulos et al. (2024b) (see Equation (A.24)).

The per-flavor neutrino luminosity per logarithmic energy is estimated as

$$\varepsilon_\nu L_{\varepsilon_\nu} \approx \frac{1}{8} f_{p\gamma}(\varepsilon_p)\, \varepsilon_p L_{\varepsilon_p}, \tag{A3}$$

where $\varepsilon_p L_{\varepsilon_p}$ is the injected proton luminosity per logarithmic energy and the neutrinos are assumed to be produced with energy $\varepsilon_\nu \sim 0.05\varepsilon_p$.

For the semianalytical calculation of the neutrino spectra in the PS and LeHa cases (displayed in Figures 9 and 10), we evaluated $t_{\rm cool}$ as described above, using as target photon fields the one computed with the code LeHaMoC. The proton loss rates for these two scenarios are presented in Figure 14. The ordering of the loss rates $t_{\rm p\gamma}^{-1} \approx t_{\rm BH}^{-1} \ll t_{\rm p,syn}^{-1}$ for $\gamma_{p,\rm max} = 10^8$ in the PS scenario is also reflected at the photon luminosity of the respective SED components (see Figure 9). For the pγ-MONOGB and pγ-PLPL cases, where only photo-meson interactions and proton escape were taken into account, the proton cooling timescale was computed as $t_{\rm cool}^{-1} = t_{\rm cross}^{-1} + t_{\rm p\gamma}^{-1}$. In all cases, $\varepsilon_p L_{\varepsilon_p}$ was described by the proton distribution used as input in LeHaMoC.

We checked that adopting a simpler, two-step function approximation for the single-pion resonance channel and the multipion channel, respectively, following the approach of A. M. Atoyan & C. D. Dermer (2003) has a negligible effect on the semianalytic results, in the sense that it is smaller than the difference between the semianalytic results and the full numerical results.

Appendix B
Additional Test Cases

B.1. Electron Cooling in the Klein–Nishina Regime

In this section, we compare the codes in their treatment of radiative losses due to inverse Compton scattering in the Klein–Nishina limit. In this regime, electrons lose a significant fraction of their energy per scattering, which can be thought of as a catastrophic energy loss process. The treatment of energy losses in the deep Klein–Nishina regime differs among the codes under comparison. Currently, LeHaMoC accounts only for cooling in the Thomson regime following Equations (42)–(43) in A. Mastichiadis & J. G. Kirk (1995). LeHa-Paris uses a continuous energy loss scheme, which was introduced by R. Moderski et al. (2005), that approximates the reduction of electron cooling in the Klein–Nishina regime.

B13 and ATHEνA use Equation (2.56) from G. R. Blumenthal & R. J. Gould (1970). In ATHEνA there is also the option to treat Klein–Nishina cooling as a catastrophic energy loss term, following Equation (2.57) from G. R. Blumenthal & R. J. Gould (1970)—see also Equation (45) in A. Mastichiadis & J. G. Kirk (1995). As a test case, we consider electrons injected into a spherical source of radius 10^{15} cm, with a power-law distribution of slope $p = 1.9$, starting from $\gamma_{e,\rm min} = 1$ and having an exponential cutoff at $\gamma_{e,\rm max} = 10^6$. The electron injection compactness is 10^{-4}.

Electrons inverse Compton scatter photons from a graybody photon field of temperature of $T = 10^6$ K and compactness of $\ell_\gamma = 100$ (or $u_\gamma = 3.7 \times 10^5$ erg cm^{-3}). The typical target photon energy is $\epsilon_{\rm GB} \sim 2.7 k_{\rm B} T \simeq 233$ eV. For the adopted parameters, electrons with $\gamma_e \ll m_e c^2/\epsilon_{\rm GB} \sim 2193$ will experience Thomson cooling, while electrons from the high-energy tail of the distribution will undergo reduced cooling due to scattering in the Klein–Nishina regime. For the purposes of this comparison, we also switch off synchrotron radiation and $\gamma\gamma$ pair production.

We present the results for this test in Figure 15. The results of B13 and ATHEνA, which are obtained using the same prescription for Klein–Nishina cooling, are similar for a wide range of Lorentz factors. In particular, their agreement is excellent (relative difference less than $\pm 5\%$) for $3 \cdot 10^3 \lesssim \gamma_e \lesssim 10^5$. The maximum difference between the two codes is $\sim$20% and is found at the cutoffs. The catastrophic-loss approximation for the Klein–Nishina cooling (dotted line) overestimates electron cooling for $\gamma_e \gtrsim 10^2$. As a result, the energy density of the steady-state electron distribution is underestimated by a factor of $\sim$10 at $\gamma_e > 10^3$. The effect on the integrated energy density of the distribution is much smaller (see blue and red bars in the right panel), as this is driven by the lowest energy particles, where both prescriptions agree well. Finally, the approximation by R. Moderski et al. (2005), which is employed in LeHa-Paris, yields similar results to the other two codes. However, it overestimates cooling at the highest energies (hence, the shift of the exponential cutoff of the distribution to lower energies), and close to the transition region between Thomson and Klein–Nishina cooling at $\gamma_e \sim 10^3$.

B.2. Monoenergetic Protons on Graybody Photons

In this section, we provide the result for the monoenergetic proton test (pγ-MONOGB) with a proton energy higher by a factor of 10 compared to the one used in the main text ($\gamma_{p,\rm min} = 10^7$, $\gamma_{p,\rm max} = 10^{7.2}$). More energetic protons interact with photons from the peak of the graybody distribution, further away from the energy threshold of the interaction. We present the results for this test in Figure 16.

As the interaction energy becomes higher, we find larger differences among the five codes. While the secondary photopion production spectra of ATHEνA and LeHa-Paris are in good agreement (see also Figure 6), the B13 spectra are systematically higher than the mean spectrum by $\sim$40% for a wide range of energies. Moreover, the spectrum of leptons from B13 appears to have a different spectral shape close to the peak. We argue that these differences arise from the different implementation methods used to compute the photopion production spectra. ATHEνA uses tabulated results of the Monte Carlo code SOPHIA and performs appropriate

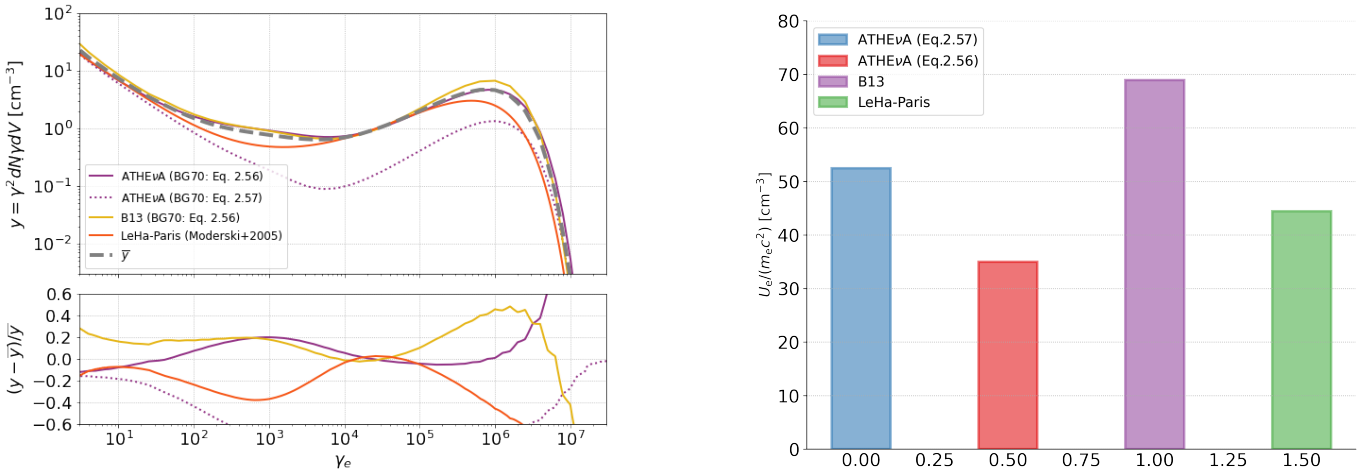

Figure 15. Effects of Klein–Nishina cooling. Left panel: steady-state electron distributions. The calculation of the average does not include the dotted curve. Right panel: integrated energy density of relativistic electrons at steady state.

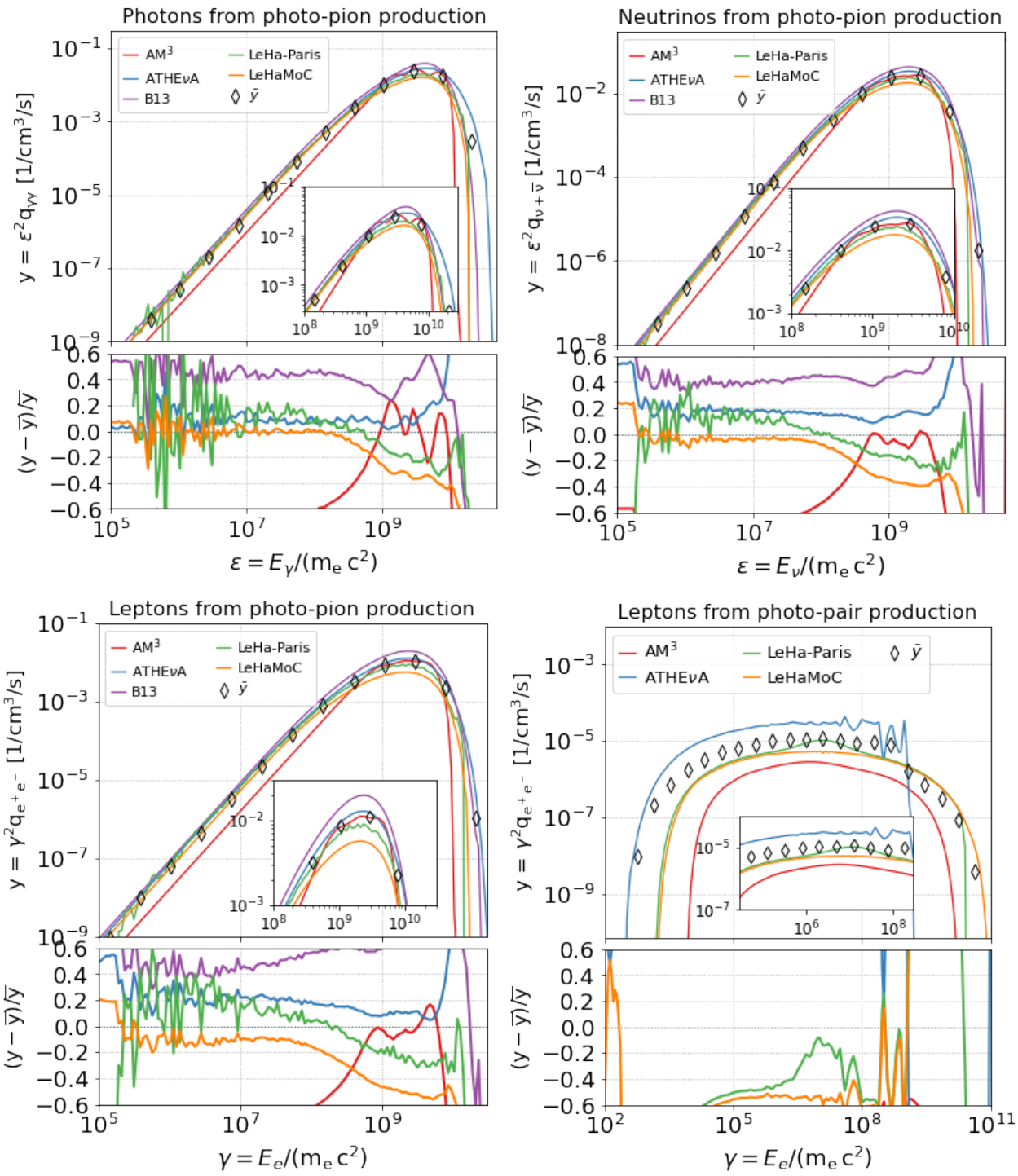

Figure 16. Same as in Figure 6 but for more energetic protons with Lorentz factors between 10^7 and $10^{7.2}$.

interpolation to match the proton and photon energy grids. LeHa-Paris actually executes SOPHIA and uses the direct output of the Monte Carlo simulation. B13 employs the formalism of S. R. Kelner & F. A. Aharonian (2008), which provides analytical parameterizations to the SOPHIA results. Inspection of Figures 1 to 3 in S. R. Kelner & F. A. Aharonian (2008) shows that these parameterizations deviate more as the energy of interaction increases. While the parameterized spectra describe very well the peak of the binned SOPHIA energy spectra, they slightly under- or overestimate the SOPHIA results away from the peak. For AM^3, the discrepancy with the other models increases at higher interaction energies for the monochromatic case, because the original approach in S. Hummer et al. (2010) not capture the interaction energy-dependence of the secondary redistribution functions very well and multipion processes play a larger role at these energies, which are more difficult to describe in terms of multiplicities and redistribution functions; see also discussion in main text. The Bethe–Heitler injection also shows a larger dispersion compared to the test with $\gamma_{p,\mathrm{min}} = 10^6$, $\gamma_{p,\mathrm{max}} = 10^{6.2}$ shown in

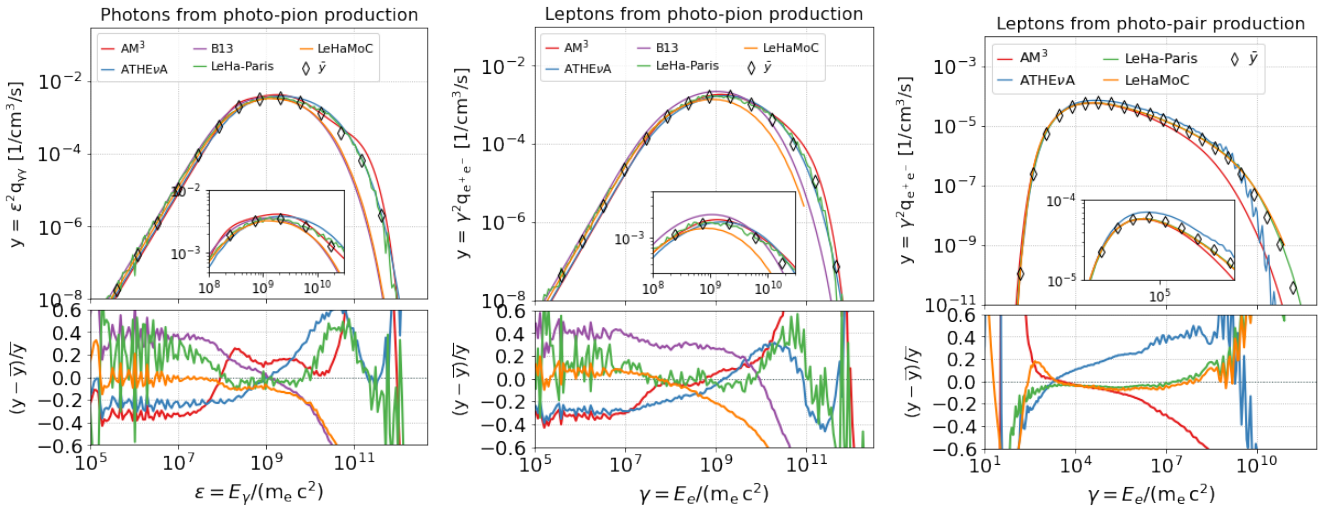

Figure 17. Production rates per unit volume of secondaries from photo-pion production (left and middle panels) and photo-pair production (right panel) for the case of a power-law proton distribution interacting with a graybody radiation field. Inset panels show a zoom into the energy range around the peak of the curves. The residuals of each code with respect to the mean value of the results are plotted in the bottom panels. The proton distribution and graybody parameters are the same as in those used in models pγ-PLPL and pγ-MONOGB, respectively (see Table 3).

the main text. In this case as well, the overestimation by ATHEνA is related to the very narrow proton distribution, as discussed in more detail in Appendix C.

B.3. Power-law Protons on Graybody Photons

In this section, we present results for interactions between power-law protons with graybody photons. The parameters used for the proton distribution are the same as in model pγ-PLPL. The graybody radiation field has the same temperature and energy density as in the pγ-MONOGB model (see Table 3). The injection rates of secondaries from photo-pion and from photo-pair production are shown in Figure 17.

Appendix C
Bethe–Heitler Numerical Implementation

The numerical implementation of Bethe–Heitler in ATHEνA is described in A. Mastichiadis et al. (2005), but some details, which are missing there, will be elucidated here. A Monte Carlo code was used to calculate the electron–positron spectra, without differentiating between electrons and positrons. Four photon energies were used as targets: $x_0 = 10^{-6}$, 10^{-4}, 10^{-2}, and 10^{0}, in units of $m_e c^2$. Those were allowed to interact with protons of energies ranging from slightly above $\gamma_p = x_0^{-1}$ (to satisfy the threshold requirement) up to $\gamma_p = 10^4\, x_0$. 25,000 interactions were performed for each energy pair, resulting in a list of interaction rates and electron–positron distributions. However, the whole list is not used in the ATHEνA code for the following reason. As we can see in Figure 18, for target photon energies of $x_0 = 10^{-6}$, $10^{-4,}$ and $10^{-2,}$ the electron–positron distributions are practically identical for commensurate proton energies (so that the interaction energy, $\gamma_p x_0$, is conserved). There is only a shift in electron–positron Lorentz factors by a factor of x_0, but once that is corrected for (right panel), the distributions are identical. The only exception to this self-similar behavior is the pair distributions produced by proton interactions with very energetic photons ($x_0 = 1$). Therefore, to save on memory, ATHEνA only uses the Monte Carlo results for $x_0 = 10^{-6}$, and when considering the interaction of γ_p protons with x photons, retrieves the electron/positron distribution from $\gamma_{p0} = \gamma_p x/x_0$ protons interacting with $x_0 = 10^{-6}$ photons. That distribution is then energy-shifted, so that any electron energy γ_{e0} will be converted to $\gamma_e = \gamma_{e0} x_0/x$. Since the Monte Carlo calculations were performed with a logarithmic step of 0.1, an interpolation is performed to obtain more accurate values of interaction rates, since photons in ATHEνA generally do not have energies in neat logarithmic multiples of 0.1. There is an obvious limitation to this method, as seen in Figure 18. The distributions are very different for the highest target photon energy ($x_0 = 1$), which serves as a target for very low proton energies. Therefore, ATHEνA simply does not consider Bethe–Heitler pair production for $\gamma_p < 10^3$, to avoid this high photon energy regime.

In LeHaMoC, the prescription of S. R. Kelner & F. A. Aharonian (2008) for the Bethe–Heitler pair spectrum (see Equation (62)) has been implemented. This is valid in the ultrarelativistic regime for protons $\gamma_p \gg 1$ and for target energy photons ϵ satisfying the following inequalities, $m_p c^2 \gg \gamma_p \epsilon \gg m_e c^2$. The computation of the innermost integral in Equation (62) of S. R. Kelner & F. A. Aharonian (2008), which involves the differential cross section, can significantly increase the simulation's execution time. To address this issue in LeHaMoC, the integral has been precalculated for various combinations of the electron and proton Lorentz factor γ_e, γ_p, and the energy of the photon in the proton's rest frame ω, drawn from a large sample, based on the parameters of each simulation. The precalculated values are then stored in an array as described in Appendix A of S. I. Stathopoulos et al. (2024b).

In Figure 19, we compare the pair production spectra obtained with ATHEνA and LeHa-Paris for proton distributions that become progressively wider in energy. We start from the effectively monoenergetic case discussed in the main text for $\gamma_p \in (10^6, 10^{6.2})$ (see $p\gamma$-MONOGB in Table 3) and decrease the lower energy of the distribution by 0.1 or 0.3 in logarithm. In all cases, the proton injection compactness (or energy density) is fixed, thus leading to a reduction of the normalization in the power-law energy spectra displayed on the right panel of the figure. We find that

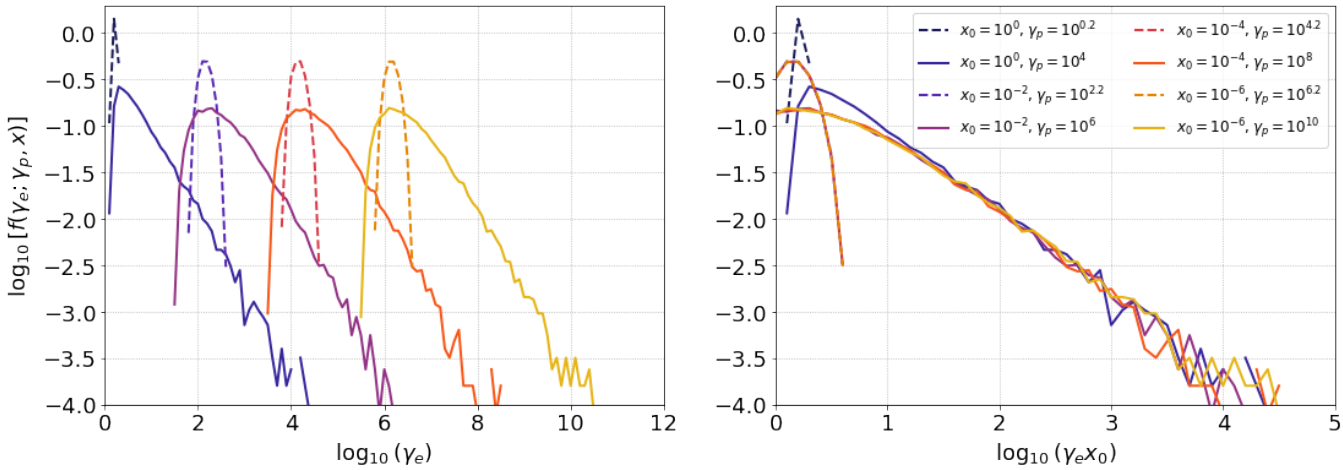

Figure 18. Left panel: electron/positron distributions, $\gamma_e\, dN/d\gamma_e$, from Bethe–Heitler pair production for various proton and target photon energies. Right panel: same as in the left panel, but after multiplying the electron/positron energies by x_0.

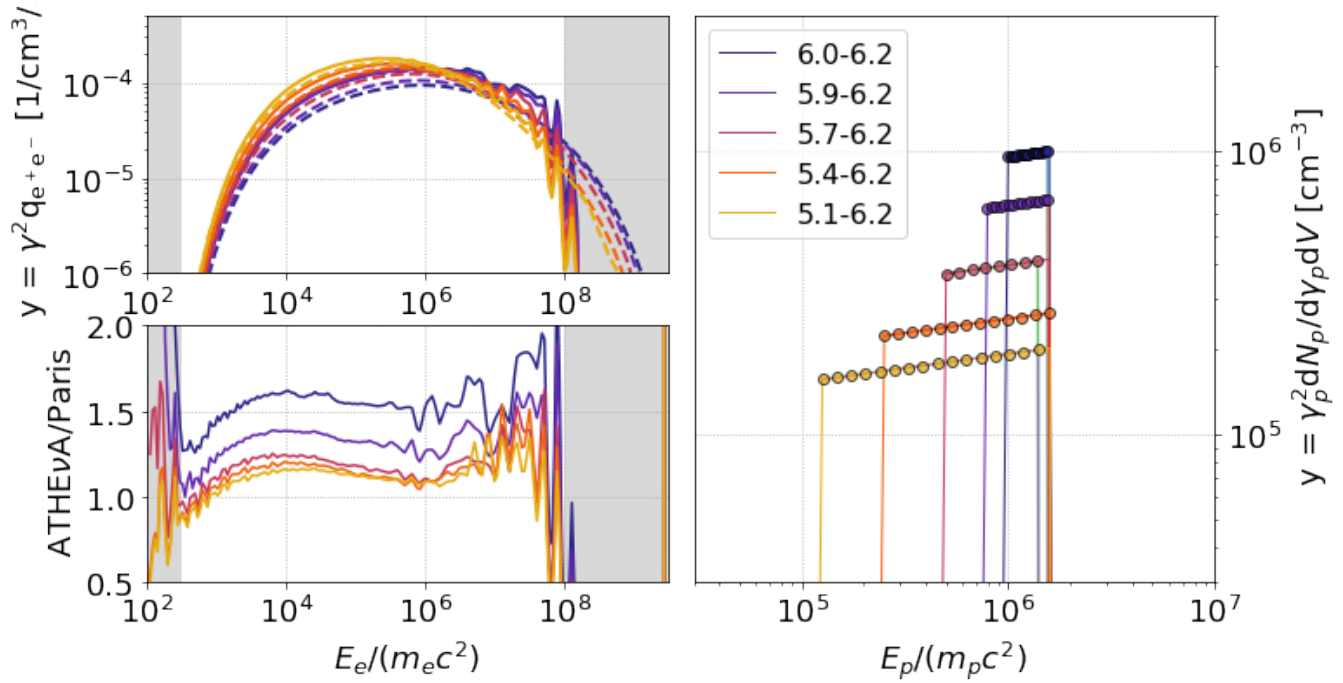

Figure 19. Photo-pair production spectra (top left) computed for interactions of protons with a progressively broader distribution (right panel) with photons from a graybody distribution of temperature 10^6 K and compactness $\ell_\gamma = 8.1 \times 10^{-6}$. The ratio of the ATHE$\nu$A and LeHa-Paris results for different pair energies is shown on the left bottom panel.

ATHEνA overpredicts the energy injection spectra by a factor of 1.5 with respect to LeHa-Paris when the proton energy distribution is very narrow, but the code results converge to a ratio of $\sim$1.1 as the distribution becomes progressively wider (left-hand side panels). We argue that these differences arise from differences in the proton energy grid resolution. The latter is fixed in ATHEνA (10 grid points per energy decade), while in LeHa-Paris the resolution is much higher (see markers on the right panel of Figure 19). To test our hypothesis, we compute the injection spectra of secondaries using the Bethe–Heitler emissivity of LeHaMoC, and the proton distributions of ATHEνA and LeHa-Paris as is. The results are presented in Figure 20. Despite the different implementations of the Bethe–Heitler emissivity among the three codes, the results are very similar when the same resolution is used for the proton distributions. While the fixed proton energy grid resolution used in ATHEνA can overestimate the injection energy for very narrow proton distributions, the code conserved energy: the energy injection rate into pairs equals the energy loss rate at every time step, thus ensuring the internal self-consistency of the numerical calculations.

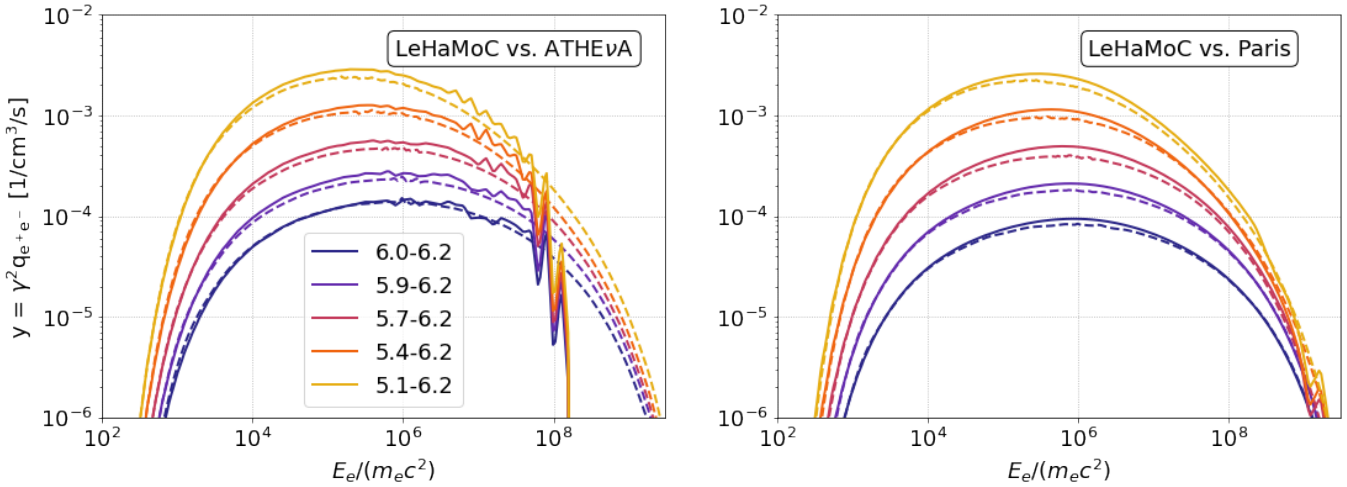

Figure 20. Photo-pair production spectra computed using the Bethe–Heitler emissivity from LeHaMoC and the proton distributions from ATHEνA (left) and LeHa-Paris (right) as is (dashed lines). Solid lines show the output of ATHEνA and LeHa-Paris codes. Starting from the bottom, each curve has been shifted vertically by a factor of 2^n for clarity purposes. All parameters are the same as in Figure 19.

ORCID iDs

Matteo Cerruti https://orcid.org/0000-0001-7891-699X
Annika Rudolph https://orcid.org/0000-0003-2040-788X
Maria Petropoulou https://orcid.org/0000-0001-6640-0179
Markus Böttcher https://orcid.org/0000-0002-8434-5692
Stamatios I. Stathopoulos https://orcid.org/0000-0002-1344-3754
Foteini Oikonomou https://orcid.org/0000-0002-0525-3758
Stavros Dimitrakoudis https://orcid.org/0000-0002-3368-3739
Anton Dmytriiev https://orcid.org/0000-0003-0102-5579
Shan Gao https://orcid.org/0000-0002-5309-2194
Susumu Inoue https://orcid.org/0000-0003-1096-9424
Apostolos Mastichiadis https://orcid.org/0000-0001-5217-4801
Kohta Murase https://orcid.org/0000-0002-5358-5642
Anita Reimer https://orcid.org/0000-0001-8604-7077
Joshua Robinson https://orcid.org/0000-0001-6399-3001
Xavier Rodrigues https://orcid.org/0000-0001-9001-3937
Walter Winter https://orcid.org/0000-0001-7062-0289
Andreas Zech https://orcid.org/0000-0002-4388-5625

References

Aab, A., Abreu, P., Aglietta, M., et al. 2020, PhRvD, 102, 062005
Aartsen, M. G., Ackermann, M., Adams, J., et al. 2014, PhRvL, 113, 101101
Abdo, A. A., Ackermann, M., Agudo, I., et al. 2010, ApJ, 716, 30
Acciari, V. A., Aniello, T., Ansoldi, S., et al. 2022, ApJ, 927, 197
Acciari, V. A., Ansoldi, S., Antonelli, L. A., et al. 2020, ApJS, 248, 29
Acharyya, A., Adams, C. B., Archer, A., et al. 2023, ApJ, 954, 70
Aguilar, M., Ali Cavasonza, L., Ambrosi, G., et al. 2021, PhR, 894, 1
Aharonian, F., Akhperjanian, A. G., Bazer-Bachi, A. R., et al. 2007, ApJL, 664, L71
Aharonian, F. A. 2000, NewA, 5, 377
Aharonian, F. A., Atoian, A. M., & Nagapetian, A. M. 1983, Afz, 19, 323
Atoyan, A. M., & Dermer, C. D. 2003, ApJ, 586, 79
Baloković, M., Paneque, D., Madejski, G., et al. 2016, ApJ, 819, 156
Banerjee, B., Macera, S., Ludovico De Santis, A., et al. 2025, A&A, 701, A68
Baring, M. G., Ellison, D. C., Reynolds, S. P., Grenier, I. A., & Goret, P. 1999, ApJ, 513, 311
Biehl, D., Boncioli, D., Fedynitch, A., & Winter, W. 2018, A&A, 611, A101
Blumenthal, G. R., & Gould, R. J. 1970, RvMP, 42, 237
Boettcher, M., Mause, H., & Schlickeiser, R. 1997, A&A, 324, 395
Böttcher, M. 2005, ApJ, 621, 176
Böttcher, M., & Dermer, C. D. 1998, ApJL, 499, L131
Böttcher, M., Reimer, A., Sweeney, K., & Prakash, A. 2013, ApJ, 768, 54
Brainerd, J. J. 1987, ApJ, 320, 714
Cerruti, M. 2020, Galax, 8, 72
Cerruti, M., Benbow, W., Chen, X., et al. 2017, A&A, 606, A68
Cerruti, M., Zech, A., Boisson, C., & Inoue, S. 2015, MNRAS, 448, 910
Cerruti, M., Zech, A., Boisson, C., et al. 2019, MNRAS, 483, L12
Chang, T., & Cooper, G. 1970, JCoPh, 6, 1
Chatzis, M., Stathopoulos, S. I., Petropoulou, M., & Vasilopoulos, G. 2024, Univ, 10, 392
Cherenkov Telescope Array Consortium, Acharya, B. S., Agudo, I., et al. 2019, Science with the Cherenkov Telescope Array (World Scientific)
Dermer, C. D., & Menon, G. 2009, High Energy Radiation from Black Holes: Gamma Rays, Cosmic Rays, and Neutrinos (Princeton Univ. Press)
Di Gesu, L., Donnarumma, I., Tavecchio, F., et al. 2022, ApJL, 938, L7
Diltz, C., Böttcher, M., & Fossati, G. 2015, ApJ, 802, 133
Dimitrakoudis, S., Mastichiadis, A., Protheroe, R. J., & Reimer, A. 2012, A&A, 546, A120
Dimitrakoudis, S., Petropoulou, M., & Mastichiadis, A. 2014, APh, 54, 61
Drury, L. O., Aharonian, F. A., & Voelk, H. J. 1994, A&A, 287, 959
Fichet de Clairfontaine, G., Buson, S., Pfeiffer, L., et al. 2023, ApJL, 958, L2
Florou, I., Petropoulou, M., & Mastichiadis, A. 2021, MNRAS, 505, 1367
Gao, S., Fedynitch, A., Winter, W., & Pohl, M. 2019, NatAs, 3, 88
Gao, S., Pohl, M., & Winter, W. 2017, ApJ, 843, 109
Gasparyan, S., Bégué, D., & Sahakyan, N. 2022, MNRAS, 509, 2102
Gould, R. J. 1979, A&A, 76, 306
Hummer, S., Ruger, M., Spanier, F., & Winter, W. 2010, ApJ, 721, 630
IceCube Collaboration, Aartsen, M. G., Ackermann, M., et al. 2018a, Sci, 361, eaat1378
IceCube Collaboration, Aartsen, M. G., Ackermann, M., et al. 2018b, Sci, 361, 147
IceCube Collaboration, Abbasi, R., Ackermann, M., et al. 2022, Sci, 378, 538
Inoue, S., Cerruti, M., Murase, K., & Liu, R.-Y. 2022, arXiv:2207.02097
Inoue, S., & Takahara, F. 1996, ApJ, 463, 555
Jiménez Fernández, B., & van Eerten, H. 2021, arXiv:2104.08207
Jones, F. C. 1968, PhRv, 167, 1159
Karavola, D., & Petropoulou, M. 2024, JCAP, 2024, 006
Karavola, D., Petropoulou, M., Fiorillo, D. F. G., Comisso, L., & Sironi, L. 2025, JCAP, 2025, 075
Kataoka, J., Mattox, J. R., Quinn, J., et al. 1999, ApJ, 514, 138
Katarzyński, K., Sol, H., & Kus, A. 2001, A&A, 367, 809
Kelner, S. R., & Aharonian, F. A. 2008, PhRvD, 78, 034013
Kelner, S. R., Aharonian, F. A., & Bugayov, V. V. 2006, PhRvD, 74, 034018
Kirk, J. G., & Mastichiadis, A. 1992, Natur, 360, 135
Klinger, M., Rudolph, A., Rodrigues, X., et al. 2024, ApJS, 275, 4
Klinger, M., Yuan, C., Taylor, A. M., & Winter, W. 2024, ApJ, 977, 242
Krawczynski, H., Hughes, S. B., Horan, D., et al. 2004, ApJ, 601, 151
Longair, M. S. 2011, High Energy Astrophysics (Cambridge Univ. Press)
Mannheim, K. 1993, A&A, 269, 67

Mastichiadis, A. 1991, MNRAS, 253, 235
Mastichiadis, A., Florou, I., Kefala, E., Boula, S. S., & Petropoulou, M. 2020, MNRAS, 495, 2458
Mastichiadis, A., & Kirk, J. G. 1995, A&A, 295, 613
Mastichiadis, A., & Kirk, J. G. 1997, A&A, 320, 19
Mastichiadis, A., Petropoulou, M., & Dimitrakoudis, S. 2013, MNRAS, 434, 2684
Mastichiadis, A., Protheroe, R. J., & Kirk, J. G. 2005, A&A, 433, 765
McEnery, J., van der Horst, A., Dominguez, A., et al. 2019, BAAS, 51, 245
Moderski, R., Sikora, M., Coppi, P. S., & Aharonian, F. 2005, MNRAS, 363, 954
Mücke, A., Engel, R., Rachen, J. P., Protheroe, R. J., & Stanev, T. 2000, CoPhC, 124, 290
Mücke, A., & Protheroe, R. J. 2001, APh, 15, 121
Mücke, A., Protheroe, R. J., Engel, R., Rachen, J. P., & Stanev, T. 2003, APh, 18, 593
Murase, K., & Nagataki, S. 2006, PhRvD, 73, 063002
Padovani, P., Alexander, D. M., Assef, R. J., et al. 2017, A&ARv, 25, 2
Padovani, P., & Giommi, P. 1995, ApJ, 444, 567
Paglione, T. A. D., Marscher, A. P., Jackson, J. M., & Bertsch, D. L. 1996, ApJ, 460, 295
Petropoulou, M., Coenders, S., & Dimitrakoudis, S. 2016, APh, 80, 115
Petropoulou, M., Dimitrakoudis, S., Mastichiadis, A., & Giannios, D. 2014a, MNRAS, 444, 2186
Petropoulou, M., Dimitrakoudis, S., Padovani, P., Mastichiadis, A., & Resconi, E. 2015a, MNRAS, 448, 2412
Petropoulou, M., Giannios, D., & Dimitrakoudis, S. 2014b, MNRAS, 445, 570
Petropoulou, M., Lefa, E., Dimitrakoudis, S., & Mastichiadis, A. 2014c, A&A, 562, A12
Petropoulou, M., & Mastichiadis, A. 2012, MNRAS, 421, 2325
Petropoulou, M., & Mastichiadis, A. 2018, MNRAS, 477, 2917
Petropoulou, M., Piran, T., & Mastichiadis, A. 2015b, MNRAS, 452, 3226
Petropoulou, M., Murase, K., Santander, M., et al. 2020, ApJ, 891, 115
Petropoulou, M., Yuan, Y., Chen, A. Y., & Mastichiadis, A. 2019, ApJ, 883, 66
Protheroe, R. J., & Johnson, P. A. 1996, APh, 4, 253
Rodrigues, X., Garrappa, S., Gao, S., et al. 2021, ApJ, 912, 54
Rodrigues, X., Karl, M., Padovani, P., et al. 2024a, A&A, 689, A147
Rodrigues, X., Paliya, V. S., Garrappa, S., et al. 2024b, A&A, 681, A119
Rudolph, A., Bošnjak, Ž., Palladino, A., Sadeh, I., & Winter, W. 2022, MNRAS, 511, 5823
Rudolph, A., Petropoulou, M., Bošnjak, Ž., & Winter, W. 2023a, ApJ, 950, 28
Rudolph, A., Petropoulou, M., Winter, W., & Bošnjak, Ž. 2023b, ApJL, 944, L34
Stathopoulos, S. I., & Petropoulou, M. 2025, MNRAS, in press
Stathopoulos, S. I., Petropoulou, M., Sironi, L., & Giannios, D. 2024a, JCAP, 2024, 009
Stathopoulos, S. I., Petropoulou, M., Vasilopoulos, G., & Mastichiadis, A. 2024b, A&A, 683, A225
Stecker, F. W. 1979, ApJ, 228, 919
Thomas, L. H. 1949, Watson Scientific Computing Laboratory Report, Columbia Univ.
Urry, C. M., & Padovani, P. 1995, PASP, 107, 803
Völk, H. J., Aharonian, F. A., & Breitschwerdt, D. 1996, SSRv, 75, 279
Vurm, I., & Poutanen, J. 2009, ApJ, 698, 293
Wang, Z.-R., Liu, R.-Y., Petropoulou, M., et al. 2022, PhRvD, 105, 023005
Yuan, C., & Winter, W. 2023, ApJ, 956, 30
Yuan, C., Winter, W., & Lunardini, C. 2024a, ApJ, 969, 136
Yuan, C., Zhang, B. T., Winter, W., & Murase, K. 2024b, ApJ, 974, 162
Zacharias, M., Reimer, A., Boisson, C., & Zech, A. 2022, MNRAS, 512, 3948
Zech, A., Cerruti, M., & Mazin, D. 2017, A&A, 602, A25
Zhang, B., & Mészáros, P. 2001, ApJ, 559, 110